UNIVERSITÀ DEGLI STUDI DI TORINO
FACOLTÀ DI SCIENZE MATEMATICHE, FISICHE E NATURALI

DOTTORATO DI RICERCA IN FISICA

XVII CICLO

Study of Heavy-Ion Reactions with the Magnetic Spectrometer PRISMA: On-line and Off-line Data Analysis

Candidate: **Andrea Latina**

Supervisors: Prof. Giovanni Pollarolo
Dott. Alberto M. Stefanini

Coordinator: Prof. Ezio Menichetti

Abstract

This study treats the problem of particle identification and data analysis in a magnetic spectrometer, PRISMA, devoted to nuclear physics experiments with heavy-ions at LNL. In this work, this problem is framed into a description of the physics purposes and the instrument in itself. Firstly, a rapid overview of the spectrometer (e.g. optics, electronics, detectors) and of the experimental methods used is given, then, the techniques for data analysis and particle identification are presented and illustrated in detail. The dissertation ends with an example of the analysis process applied to the data set from the 505 MeV ^{82}Se+^{238}U reaction, which was recently studied at LNL, and where transfers of several nucleons were observed.

PRISMA has an entrance solid angle of 80 msr and can identify each nucleus, unambiguously, in the whole Chart of Nuclides. These peculiar characteristics of the spectrometer, together with the features of the accelerator complex of the LNL, make it very suitable for studies of heavy-ion reactions, including the processes, known as the grazing reactions, where the projectile and the target interact gently with each other. Multi-nucleon transfer reactions, where cross sections may be very small, can be studied with PRISMA.

In order to allow this, one needs to track the trajectories of the ions passing through the spectrometer. The algorithms for full ion tracking must reconstruct the trajectories from the target to the focal plane detectors, by taking into account both the exact optics of the magnets and the geometry of the instrument. This method requires a lot of computational power. A simple and fast, but less accurate, geometrical method is presented as well.

The full ion tracking allows also to calculate the velocity vector at any point of the trajectory. This information is necessary to apply the Doppler corrections, in nuclear spectroscopy experiments, when PRISMA is coupled with an array of γ-detectors, such as CLARA.

Acknowledgments

I am grateful to my supervisors Dr. Alberto Stefanini and Prof. Giovanni Pollarolo that they have given me the opportunity to work with them. Their engaged support, guidance and help throughout this project contributed greatly to its success.

During the project Dr. Fernando Scarlassara has been a continuing source of inspiration and ideas. For these contributions and for the numerous and pleasant discussions we had, I thank him. I am also grateful to all the members of the PRISMA group: Dr. Giovanna Montagnoli, Dr. Monica Trotta, Dr. Lorenzo Corradi, Dr. Silvio Beghini and Dr. Enrico Fioretto for their enthusiasm and professionalism. I would like also to mention the post-docs I had the chance to meet along these years, Dr. Suzana Szilner and Dr. Bivash Ranjan Behera, they have been not only precious collaborators but also good friends. I am also sincerely thankful to all the members of the GASP-CLARA group, in particular Dr. Andres R. Gadea, Dr. Daniel Ricardo Napoli, Dr. Giacomo De Angelis, Dr. Enrico Farnea and Dr. Nicu Marginean, their professionalism and personal warmth have made working with them an unforgettable experience. Finally, I would like to thank the technical and administrative staffs of Laboratori Nazionali di Legnaro, without whom my experience would not have been so positive, and this work not possible.

Greatly acknowledged is the receipt of a scholarship grants from the National Italian Nuclear Physics Institute.

Contents

Chapter 1

Heavy-Ion Magnetic Spectrometers

1.1 Magnetic Spectrometers

Magnetic spectrometers have been very powerful instruments of research since the beginning of experimental nuclear physics. In some case even necessary, when the energy resolution was important or it was difficult to suppress the background. For many years experimentalists have been committed to design best characteristics of the spectrometer such as: good optical properties, good energy resolution and background suppression etc.

Nowadays, magnetic systems serve many essential purposes in nuclear laboratories, particularly in the preparation of high-quality accelerator beams and in the analysis of complex spectra from nuclear reactions. The technology of magnetic spectrograph design and construction has advanced greatly. Exploitation of fringe-field focusing and many-element design with multi-pole lenses has produced improved resolution and two-dimensional focusing. Well-known types are the Enge split-pole magnet and the family of Q3D magnets. A review of magnetic spectrographs can be find in [12]. The characteristics of several types are given in Fig. 1.1.

As reaction products analyzers, magnetic spectrographs offer the advan-

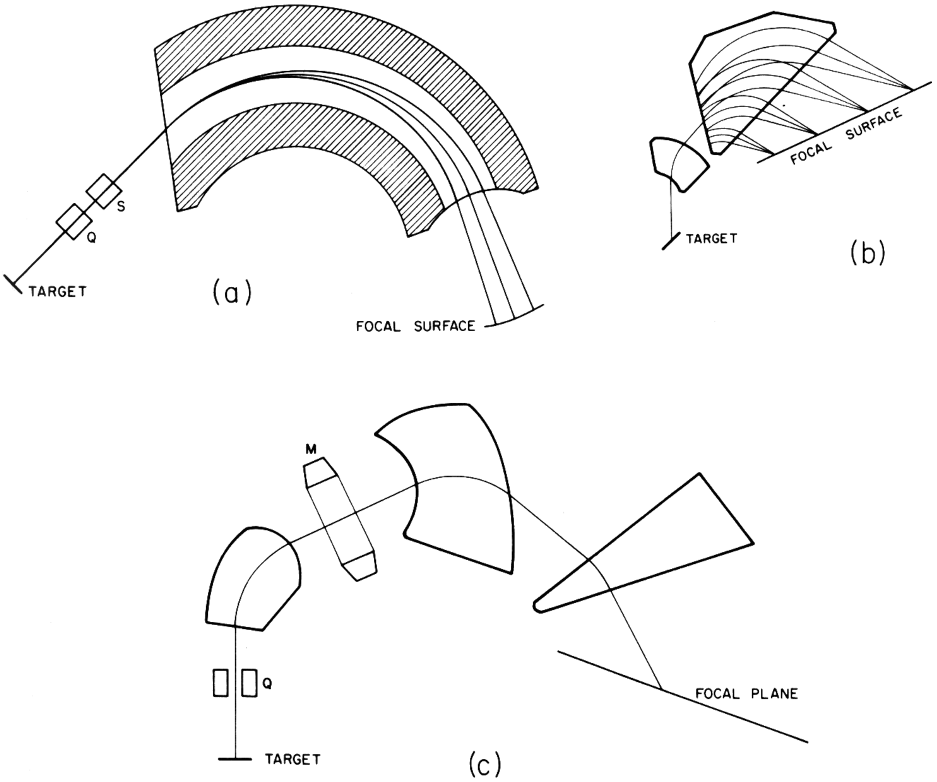

Figure 1.1: *Diagrams illustrating several magnetic spectrometer designs: (a) from Berkeley 88-in Cyclotron Laboratory; (b) Enge split-pole type; Strasbourg Q3D (QWTH) type with flat focal surface. Q, quadrupole; M, multi-pole; S, sextupole. Focusing is shown only in (b).*

tages of high resolution and large solid angle of acceptance and they allow the deflection of unwanted particles away from the open window of the focal plane detector. The radius of curvature of an ion in the magnetic field is given by

$$\rho = \frac{p}{qeB} \tag{1.1}$$

where p is the momentum, qe is the ionic charge and B is the magnetic induction. In magnetic spectrometers the information about the mass and the energy of the ions is extracted by measuring their position on the focal plane and their time of flight inside the instrument. Formerly, several spectrometers have been designed explicitly for heavy ions (e.g. Jaeri [23], GSI [37]), but, since their optical aberrations could be corrected only by hardware, they had a very small entrance solid angle. The project for the spectrometer SUSAN [8], at Daresbury, has represented a big improvement in this field: its entrance solid angle was 10 times larger than any other spectrometer with conventional optical corrections. Unfortunately, SUSAN was never constructed.

1.1.1 Properties

The properties of a magnetic spectrometer lie in its focal plane detection system and in the optical properties of the magnets, especially the length, width, and curvature of the focal surface, the range of the angles of incidence of the particles at the focal surface, and the line-width limit inherent in the electron optical design.

Here are briefly reviewed the properties of the magnetic spectrographs shown in Fig. 1.1. The nominal 41^o and 45^o angles of incidence of the split-pole and Q3D magnets are excellent for a photographic plate recording detection system, because they produce tracks easily counted under the microscope. On the other hand, the normal angle of incidence of the Berkeley magnet [20] is superior for those position-sensitive detectors which give best spatial resolution with particles arriving at $\theta = 0^o$. Finally, the curvature of the focal surface of the split-pole spectrograph and some Q3D types may cause little troubles with the detection system. These spectrometers in fact would require detectors conform to the focal surface, but it can be a problem for some types of detectors to be designed curved. In practice flat counters shorter than the overall length of the focal surface are often used, placed so as to keep the maximum deviation of the counter axis from the focal surface small. The Q3D magnets at Groningen and Strasbourg have flat surfaces facilitating the design of long detectors. In other q3D series magnets, the focal surface radius of curvature is about 2.4 to 3.2 times the mean projectile path radius of curvature ρ_0. In those cases broad-range, in absence of automatic event-by-event correction, detectors should be curved.

Aberrations inherent in the optical deign set an ultimate limit on the sharpness of focusing. Under the assumption of a 1-mm-wide target spot and negligible target thickness and beam energy spread, at the midrange radius ρ_0 the inherent line-width limit is roughly 0.3 mm for the split-pole spectrometer and 1 to 1.5 mm for Q3D types. These numbers correspond to moderate openings of the spectrographs entrance slits; they become larger or smaller as the slit opening increases or decreases. Severe broadening occurs when the slit becomes wider than the maximum design limit; in these cases are necessary systems with event-by-event correction via *ray tracing*.

1.1.2 Ray Tracing

Ray-tracing, which can be done if two points sufficiently separated along the track can be determined [13], offers valuable possibilities [17]:

1. Correction of optical aberrations, permitting the use of solid angles much larger than the normal design. In some cases y coordinates as well as x coordinates may be needed;

2. Correction of possible curvature of the focal surface;

3. Correction of the path differences in the time of flight work;

4. Simultaneous observation of a reaction at many scattering angles. This is especially useful in heavy-ion experiments, where cross section often varies rapidly with scattering angle;

5. Elimination of impurity lines. In favorable cases the focal surface for an impurity spectrum, and for the spectrum of interest, lie so well separated from one another that a sharp line in either will be seen as a broad band in the other; then the data processing computer can be programmed to find the intersection of all rays with the impurity focal surface and to reject all which pass with in a specified short distance of

the position of known impurity lines. The wider the spectrograph entrance slits are, the smaller will be the correction required for particles eliminated from the desired spectrum.

1.1.3 Modern Spectrometers

In modern spectrometers (PRISMA[41], Vamos[36]), refined detectors and ion track reconstruction have a key role. High-resolution detectors can compensate approximated optical properties because the aberrations can be corrected during the analysis by a computer reconstruction of the trajectories. This allows constructing spectrometers with wider angular acceptances, so wide as it never has been thinkable in the past. Surely, this trend has been also favored by the recent developments in fast multi-parametric acquisition systems as well as in copter performances in general. This permits to acquire and to analyze big quantities of data in a reasonable amount of time.

This frame fits with PRISMA and the heavy ions reactions of interest at LNL, where the collisions between the beam and the target, usually generate many reaction products, with possibly very low cross sections, whose identification is much more difficult than with light ions. Moreover, in case of heavy ions, the ion charge state q distribution complicates the situation. Position spectra on the focal plane are in fact an overlap of q and mass A distributions with different energies. In this case, the dispersion on the focal plane is no longer enough to identify the reaction products, i.e. to determine, unambiguously, their nuclear charge Z and atomic mass number A. Therefore, one must measure additional quantities such as the time of flight and an accurate $\Delta E/E$. For these reasons and in order to measure very weak reaction channels embedded in a huge background of elastically scattered ions, very high quality detectors are required.

For the sake of completeness, it is well known that a combination of magnetic and electric fields induces a spatial dispersion of the ions with different masses along the focal plane. Instruments based on this principle are called recoil-mass spectrometers and several spectrometers of this kind have been built and operated in recent years, including CAMEL at Legnaro [38], the FMA at Argonne [3], the Oak Ridge RMS [18], HIRA at NSC New Delhi [39], the JAERI RMS [23], and DRAGON at TRIUMF [22]. These instruments are frequently used at 0^o or small angles to identify the resulting particles of fusion-evaporation reactions; their limits are the small entrance solid angle (a few msr, but actually the evaporation products are focused forwards) and the maximum electric rigidity which can be analyzed. For instance, RMS, the recoil mass spectrometer of LNL, can analyze only fragments with an electric rigidity up to 7-8 MeV/q, whereas quasi-elastic reactions produce fragments with rigidities of 15-20 MeV/q, even with beams with masses 80-100, already at energies near the Coulomb barrier.

1.2 Heavy-Ion Transfer Reactions

In all heavy-ion experiments near and above the Coulomb barrier, one has been able to identify a characteristic type of reaction products where the projectile has lost only a moderate amount of energy and has exchanged only a few nucleons with the target nucleus. These reactions are called quasi-elastic reactions and are assumed to correspond to collisions in which the surfaces of the two ions have just been in grazing contact (i.e., the *grazing reactions*).

The grazing reactions, for their simplicity, permit to find the main degrees of freedom which are excited in the collision. Among them, an interesting field of research is covered by the *multinucleon transfer reactions*. Studying this type of reactions it is possible to investigate the correlations between nuclear dynamics and nuclear structure effects, although theoretical analysis of these reactions have only been performed with relatively light projectiles where the effects associated with Coulomb excitation are of minor importance.

We consider such grazing reactions where the trajectory of relative motion can be described by the classical trajectory in the combined field of Coulomb repulsion and a nuclear attraction and where the depopulation of the ground state is accounted for by absorption.

In many cases, an enhancement has been observed in the cross sections of a pair of particles with respect to the sequential transfer of single nucleons. Nevertheless, a complete analysis of these data has not been possible, with the present instruments, and it has not been possible to verify quantitatively the effect of pair correlations and how they influence the reaction. In order to understand these aspects, it is necessary to measure the transfer of several pairs with a very good resolution in charge (Z), mass (A) and Q-value. Multiple transfer of nucleons has already been observed in many cases: e.g., grazing reaction between heavy ions at energies 10 or 20 % above the Coulomb barrier, in deep-inelastic scattering reactions, but usually with a poor resolution in Z and no resolution in mass or energy at all.

A detailed study of such reactions, where transfer of several nucleons takes place at energies where effects of nuclear structure still dominate, is missing. From a theoretical point of view we can only treat in detail the transfer of a single nucleon or, introducing a proper macroscopic form factor, the transfer of two nucleons. When the number of transferred nucleons increases, the calculations get extremely complex and, for this reason, the theoretical studies of this phenomenon have been limited for several years.

1.3 Recent achievements in multinucleon transfer reaction studies at LNL and present perspectives with PRISMA

Transfer reactions between heavy ions provide important information for both nuclear structure and reaction dynamics studies. In a single particle transfer one can deduce shell properties of nuclei populated via stripping and pick-up of neutrons and protons. In the transfer of two nucleons one can investigate nucleon correlations, pairing in particular. In multinucleon transfer one can study the important degrees of freedom acting in the transfer process, namely single nucleon, pair or even cluster transfer modes, and how they evolve as a function of the transferred nucleons.

An extensive work using different heavy ion reactions was performed during last years at LNL, using the PISOLO detector [31]. PISOLO is a time of flight spectrometer, which has been operating in the LNL during the last decade, whose characteristics are: magnetic focusing, solid angle ≃3 msr, mass resolution $\Delta A/A \simeq 1/100$, nuclear charge resolution $\Delta Z/Z \simeq 1/50$. See Fig. 1.2 for a schematic picture of the set up. The variety of channels which could be observed in several experiments allowed to follow in a systematic way the population pattern of the reaction products in the Z-A plane. Parallel to this experimental work, semi-classical theories have been developed, and new models have been implemented treating quasi-elastic and deep-inelastic processes on the same ground. This allows a meaningful quantitative comparison with the experimental observables.

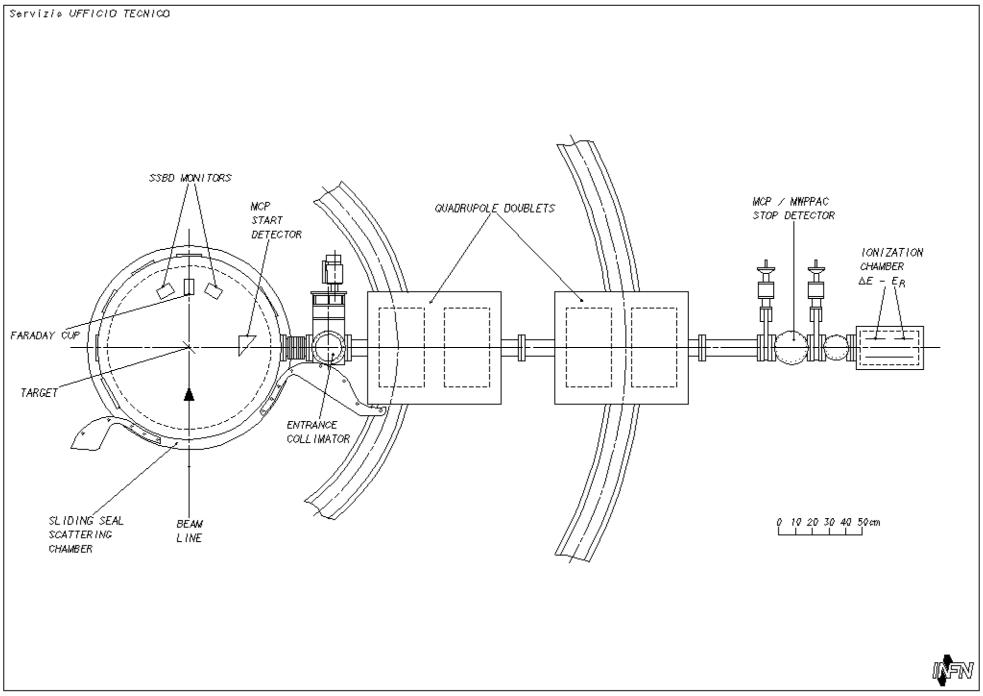

Figure 1.2: *The time of flight spectrometer PISOLO[31]*

multinucleon transfer reactions constitute also a valuable tool to populate neutron-rich isotopes, at least in specific mass regions. The study of the lowest excited levels of neutron-rich nuclei is an area of increasing interest since one gets information on changes of shell structure and on the behavior of nucleon correlations in unexplored mass and spin regions. A very powerful technique is coupling large γ-detector arrays with the new generation large solid angle spectrometers.

Comparing one- and two-particle transfer processes one can learn a lot on the interplay between single nucleon and pair transfer modes, but it is only when several nucleons get transferred that one has a better view on how the mechanism evolves. An example of a complete measurements performed with the TOF spectrometer PISOLO is that for the ^{58}Ni+^{208}Pb system. The experimental total angle- and Q-value integrated cross section for pure neutron pick-up and pure proton stripping channels are reported in Fig. 1.3 and are compared with calculations performed within the semi-classical Complex WKB (CWKB) model (see [10] and references therein for details).

The experimental data show a quite regular drop of the cross sections as a function of the number of transferred nucleons, indicating that the transfer mechanism likely proceeds as a sequence of independent particle modes. Similar results have been obtained at Argonne [24]. With the dotted line of Fig. 1.3 we show the calculations made treating the transfer in a successive approximation considering all the transition as independent. A good agreement between data and theory is obtained for the case of pure neutrons and for channels involving the stripping of one proton. However, as more proton are transferred, the calculations are not able to follow the trend of the data. The discrepancies indicate that degrees of freedom beyond single-particle transfer modes have to be incorporated in the theory, or that more complex processes, i.e., deep inelastic components, play an important role. Adding into theory the transfer of a pair of protons and fixing the strength of the macroscopic form factor to reproduce the pure $-2p$ channel, one sees (dashed line) that the predictions for the other charge transfer channels are also much better.

However, the treatment of this pair mode is only at a phenomenological level due to the well known difficulties to relate microscopically its strength to the pair correlations in target and in projectile. For the pure neutron transfer no pair mode was included and the cross section represented by the dashed and the dashed-dotted lines (not shown) are very close to the full line. In multinucleon transfer channels large energy losses show up, therefore the final yield can be considerably altered by evaporation. Including these evaporation effects in the calculation the final cross sections are shown as full lines in Fig. 1.3.

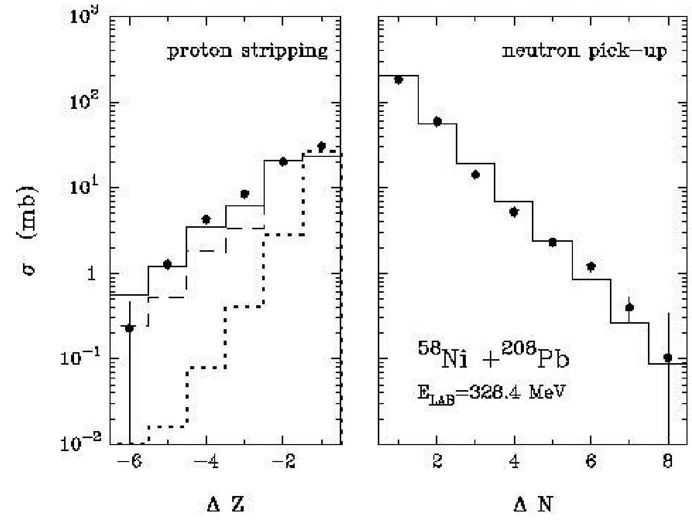

Figure 1.3: *Total cross sections for pure proton stripping (left side) and pure neutron pickup (right side) channels for the indicated reaction. The lines are the CWKB calculation (see text).*

In heavy-ion transfer reactions the strong Coulomb interaction favors inelastic excitations and an interesting question is to what extent pair correlations play a role at high excitation energy. To answer this question is not an easy task since several effects are mixed up, for instance it is not clear if the pair transfer proceeds in a cluster- or sequential-like picture. For the system ^{62}Ni+^{206}Pb, cross sections have been measured at three bombarding energies up to three nucleon pairs (here all pure neutron channels have well matched

Q-values). Only the $+1n$ and $+2n$ channels have the main population close to the Q-value corresponding to nucleon transfers between ground states ("ground-to-ground"). More massive transfer channels display a population towards more negative Q-values, with a tail increasing with the number of transferred neutrons. The observation of these long tails suggests that contributions from "cold" transfers, associated with low excitation energy, is likely hidden by dominant "warm" sequential transfer processes.

On the other hand a significant fraction of the flux remains close to $Q \approx 0$ up to the $+4n$ channel. This indicates that experiments with higher energy resolution may be able to distinguish the population to the ground state from the flux going to excited states, thus giving better signatures of the transfer contribution coming from pair modes.

Further interesting results from Q-value distributions come from the study of ^{40}Ca+^{208}Pb, where both projectile and target are magic (double closed-shell nuclei) and therefore provide an excellent opportunity for a quantitative comparison with theoretical models. Fig. 1.4 shows TKEL distributions at the three measured bombarding energies for the two neutron pick-up channel together with CWKB calculations. As can be appreciated, the two neutron pick-up channel displays at all measured energies a well defined maximum, which, within the energy resolution of the experiment, is consistent with a dominant population, not of the ground state of ^{42}Ca, but of the excitation region around 6 MeV. The final population of the single particle levels used in the CWKB theory suggests that the maxima are essentially due to two neutrons in the $p_{3/2}$ orbitals. This corresponds to the excited 0^+ states that were interpreted as multi (additional and removal) pair-phonon states. If so, these results show that, at least in suitable cases, one can selectively populate specific Q-value ranges even in heavy-ion collisions, opening the possibility to study multi pair-phonon excitations. The strong concentration near 6 MeV of excitation energy of these peculiar 0^+ states for ^{42}Ca is clearly visible in the bottom part of Fig. 3, where the strength distribution $S(E)$ performed in the framework of large scale shell model (SM) calculations is shown [42].

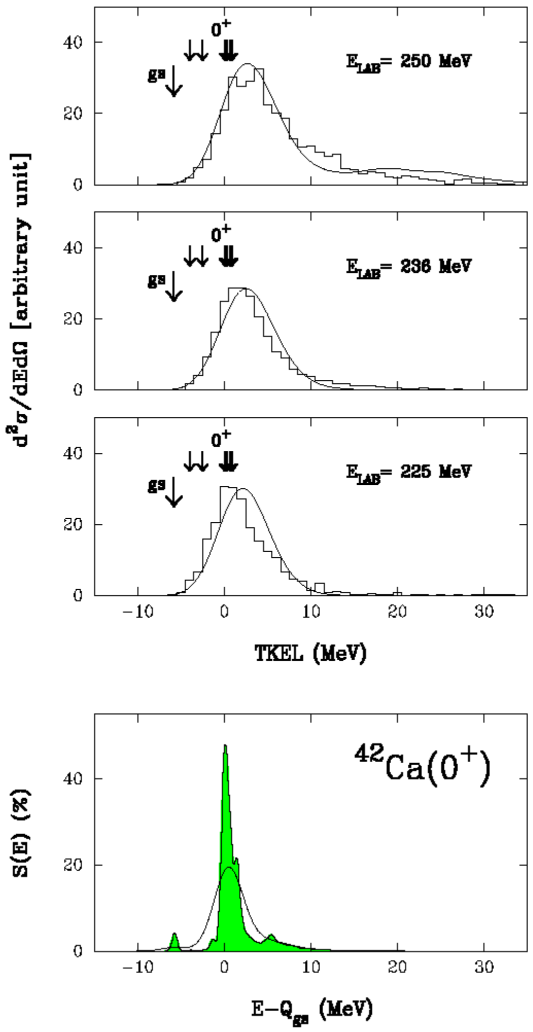

Figure 1.4: *Experimental (histograms) and theoretical (curves) total kinetic energy loss distributions of the two neutron pick-up channels at the indicated energies. The arrows correspond to the energies of 0^+ states in ^{42}Ca with an excitation energy lower than 7 MeV. Bottom panel shows the strength function $S(E)$ from shell model calculations (see [42] for details).*

As can be argued from the results presented above it would be important to distinguish the population to specific nuclear states and to determine both their strength distribution and decay pattern. This, in fact, carries information on the wave-function components of the populated levels and therefore also on the pairing correlation [6]. Experiments in this direction must exploit the full capability of spectrometers with solid angles much larger than the conventional ones, and with A, Z, and energy resolutions sufficient to deal also with heavier mass ions. This is possible now with the PRISMA spectrometer. First experiments on heavy-ion grazing collisions have been already performed with beams in the A=40-90 mass range.

A further interesting issue is studying nuclear structure of neutron-rich nuclei, populated of relatively high angular momentum, by means of binary reactions. These studies have been initiated by combining PRISMA with the CLARA gamma-array [14], recently installed close to the target point and consists of an array of 24 Clover detectors (from the Euroball collaboration). With stable beams at energies and intensities typical of tandem accelerators, one can presently reach regions moderately far from stability (about 3-5 nucleons from the last stable isotope), and one can investigate nuclei through the entire nuclear chart, by suitable projectile/targets combinations.

Chapter 2

The Magnetic Spectrometer PRISMA

PRISMA is a magnetic spectrometer recently installed at the Legnaro National Laboratories (LNL), born by a collaboration between the Universities of Padua, Turin, Naples and the LNL themselves. PRISMA fits with the physics scenario described in the previous chapter. It has been designed for the identification of nuclei produced in heavy-ion binary reactions at energies E=5-20 MeV/A, like those of the XTU Tandem-ALPI-PIAVE accelerator complex of the LNL[28]. The spectrometer's characteristics make it suitable for experiments in the field of reaction dynamics at low energies as well as for nuclear structure studies, when coupled with a modern array of γ-detectors, such as CLARA [14], temporarily operating in conjunction with PRISMA until the end of 2006. The spectrometer will permit also to exploit the features of the proposed radioactive beam facility SPES[40, 1].

The PRISMA project was first funded by INFN in 1998, its real construction begun in 2000 (when magnets have been delivered to LNL) and the full set-up was completed before the end of 2003.

The year going from Summer 2003 to Summer 2004 has been the first of full operation of the spectrometer. Various experiments, in the fields of few- and multinucleon transfer between heavy ions, have been performed. This chapter reviews the main characteristics of PRISMA and its detectors.

Characteristics of PRISMA	
Solid angle	80 msr
Energy acceptance	± 20%
Resolving power	$p/\Delta p \simeq 2000$
Mass resolution	1/300
Energy resolution	up to 1/1000
Z resolution	1/60
Kinematic correction	via software
Aberration correction	via software
Dispersion	4cm/%
Count rate capability	up to 50-100 KHz

Table 2.1: *Characteristics of PRISMA.*

2.1 Description

A picture of the spectrometer is shown in Fig. 2.1. The spectrometer's features are summarized in Tab. 2.1. Such performances are achieved by software reconstruction of the ion tracks using the position, the time of flight and the energy loss information provided by the entrance and focal-plane detectors. The spectrometer consists of a dipole with a quadrupole lens for vertical focusing. Its optics is described in the next section. In the design of PRISMA, detectors are very important. The PRISMA detectors are three: the entrance detector based on micro-channel plates (MCP), the multiwire PPAC (MWPPAC) detector and the ionization chamber at the focal plane. The time of flight information comes from the delay between the signals derived from the entrance and the MWPPAC detectors. Since the focal plane detector is at a large distance (≈ 6.5 m) from the entrance detector, the time of flight is typically quite large ($200 - 400$ ns), and this allows to have a very good

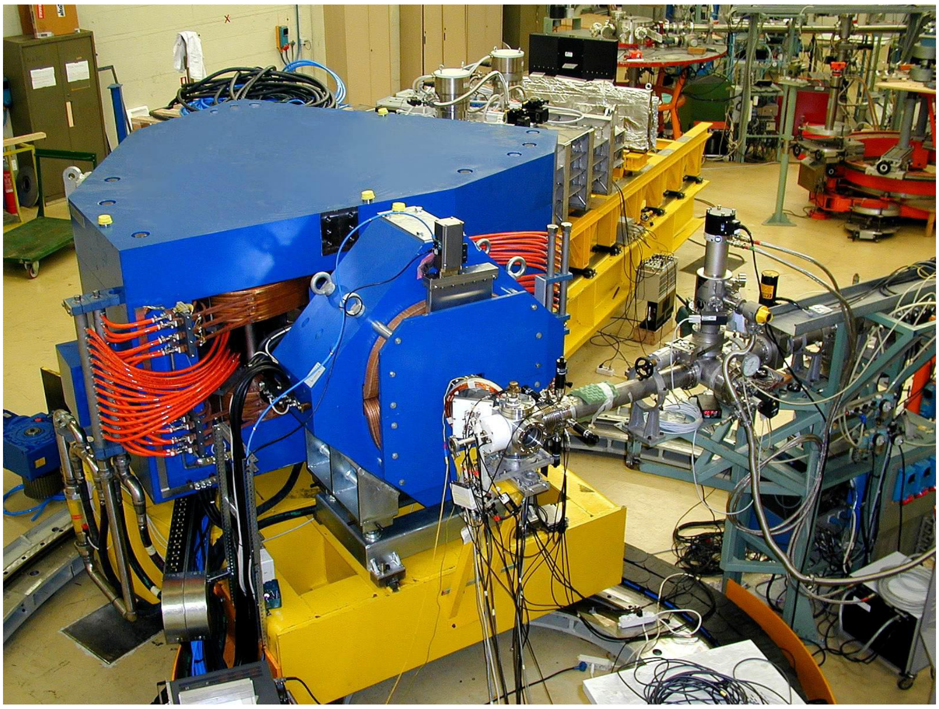

Figure 2.1: *The PRISMA magnetic spectrometer*

resolution in the time of flight measurement. The entrance MCP detector is mounted between the target and the quadrupole magnet; it gives the position information for both X and Y coordinates (with better than 1 mm FWHM resolution), on a sensitive area 80×100 mm^2. The MWPPAC, a gas-filled multi-wire proportional counter, is placed 323 cm away from the exit of the dipole; it also gives both the X and Y coordinates (with 1 mm of resolution) on a detecting area 100 × 13 cm^2. An array of ionization chambers, for energy and energy loss measurements, is placed beyond the MWPPAC, 72 cm away from it.

2.2 Ion Optical Elements

The optics of PRISMA consists of a quadrupole singlet and a bending dipole. The quadrupole lens is mounted 50 cm away from the target, and its main

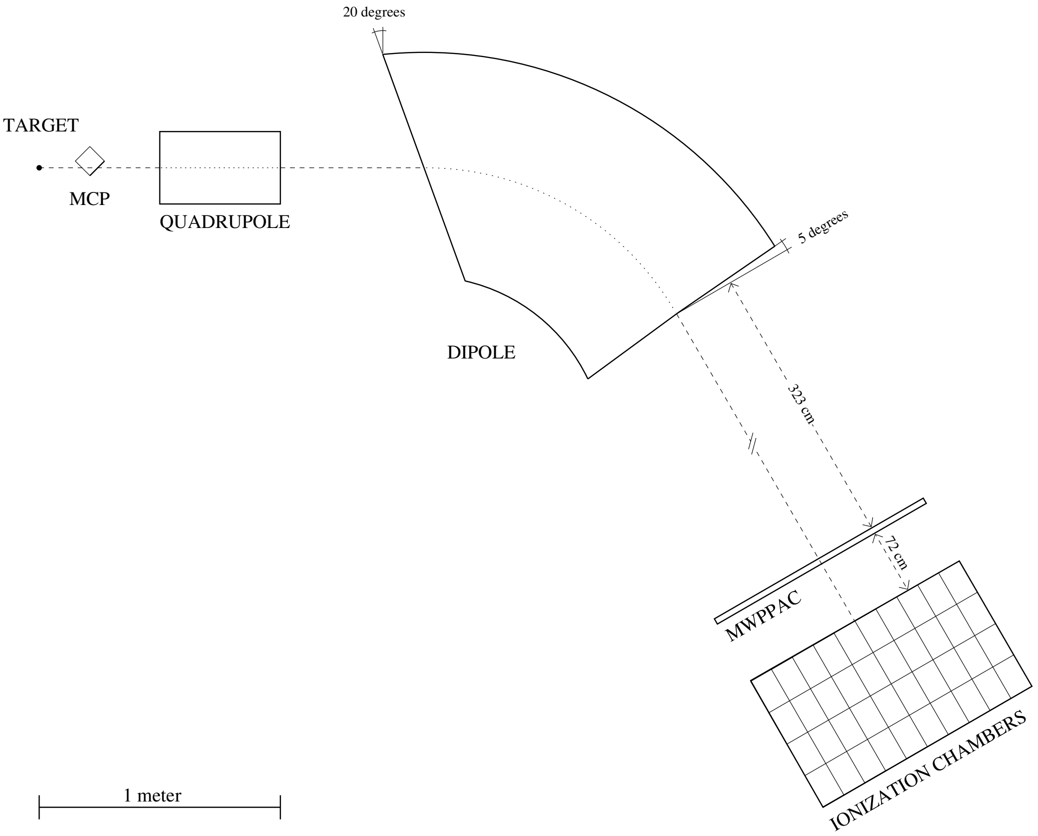

Figure 2.2: *The PRISMA magnetic spectrometer*

purpose is collection efficiency. Its aperture diameter is 32 cm and its effective length is 50 cm. It must be noticed that the ratio, length over diameter,

$$\frac{L}{D} \approx 1.5,$$

is slightly below the limit for the fringing field domination, so that the fringe field is small enough compared to the inner field. This magnet focuses in the vertical (Y) direction and defocuses in the horizontal (X) direction (see Tab. 2.2).

The dipole magnet is placed 60 cm downstream of the quadrupole. It is of the uniform field type and has a bending angle of 60^o for the central trajectory. The bending radius is 1.2 m and the maximum B is 1 T, which corresponds to a maximum rigidity of 1.2 T m ($B\rho = 1.2$ T m). The pole gap is 20 cm and the entrance and exit widths are 1 m. The entrance effective field boundary (EFB) forms an angle of -20^o at the entrance and $+5^o$ at the exit. The main reason for this choice is to maximize the transmission and the resolution (see Tab. 2.3). Simulations of the PRISMA optical properties are visible in Fig. 2.3.

The magnetic rigidity of 1.2 T m has been calculated in order to be able to exploit the specific characteristics of the LNL ALPI-Tandem complex, where ions up to an energy of 5-10 MeV per nucleon can be accelerated, for ions up to ^{208}Pb.

QUADRUPOLE		
Max. field gradient	G	5.3 T/m
Max. pole tip field	B_0	0.848 T
Effective length	l_{eff}	500 mm
Aperture diameter	d	320 mm
Pole profile		Multi-faceted
Yoke shape		Square

Table 2.2: *Characteristics of the PRISMA Quadrupole Magnet.*

DIPOLE		
Maximum field	B	1.0 T
Bending radius	R_0	1200 mm
Bending angle	ϕ	60°
Entrance angle	ϵ_1	-20°
Exit angle	ϵ_2	+5°
Pole gap	d	200 mm
Homogeneity at the Center		1×10^{-3} over $+500/-400$ mm

Table 2.3: *Characteristics of the PRISMA Dipole Magnet.*

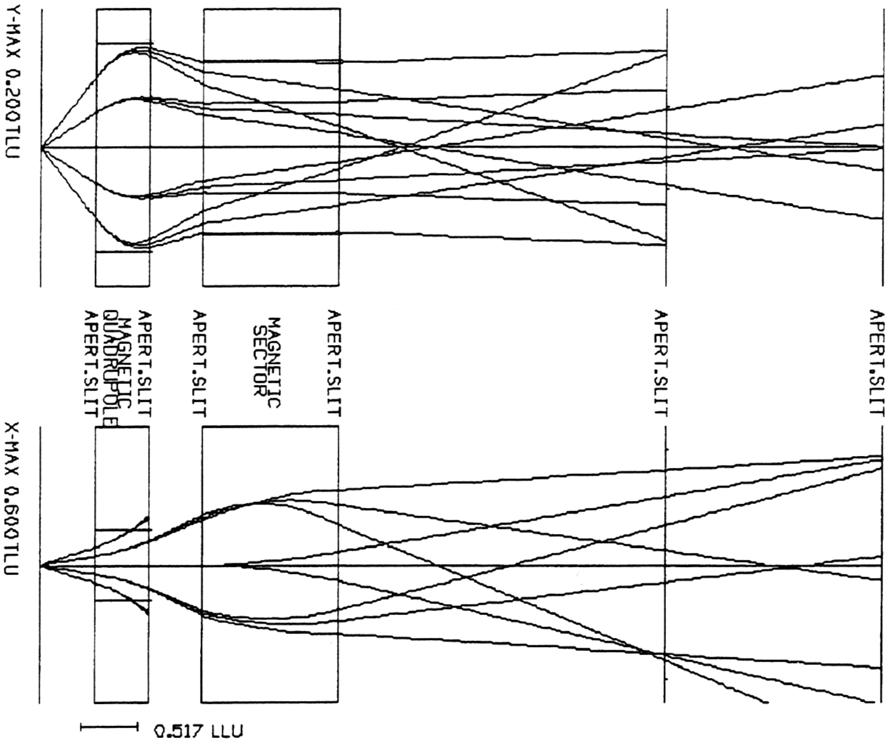

Figure 2.3: *Trajectories calculated with GIOS[26], for particles of mass 58 and charge 28 passing through PRISMA at 15 MeV/nucleon,* $\pm10\%, \pm20\%$.

2.3 Detectors and Electronics

2.3.1 The Entrance Detector

The entrance detector for the PRISMA spectrometer has to provide time and position information in both X (along the dispersion plane) and Y directions with minimum scattering. It was designed and constructed in a collaboration between Padua and LNL.

The detecting surface of the detector is based on large area Micro-Channel Plates (MCP). The active area of the MCP is 80×100 mm^2, and covers the whole solid angle of PRISMA at 25 cm from the target. A thin Carbon foil ($\simeq 20\mu$g/cm^2) is passed by the particles at an angle of 135^o. The backward emitted secondary electrons are accelerated towards the MCP by an electrostatic field (up to $\simeq$ 300 eV) and spiraled by a parallel magnetic field produced by an external coil ($\simeq$ 120 Gauss), which limits the spread of the electron cloud, preserving the particle position information [34]. The electric field between the Carbon foil and the accelerating grid (placed at $\simeq$ 1 cm) has typical values of 30-40 kV/m. The front surface of the MCP is at the same potential as the accelerating grid.

The anode structure for X, Y readout is made of two orthogonal delay lines, wrapped around rounded plastic frames of two different diameters to keep the two lines insulated from each other and both from the inner metallic plate. The delay lines are homemade using Cu-Be wire 70 μm diameter. The charge coming out from the MCP is shared between the two delay lines thanks to a suitable DC-voltage adjustment. Each delay line consists of two windings with 1 mm pitch and only one collects the charge. The two windings are connected on one side to low-noise differential amplifiers, while on the other end they are grounded. Position information is obtained from the difference in arrival time of the signal at one end of the delay line with respect to a fast time signal independently derived from the output face of the MCP pair. This fast signal is used both as reference signal for the X, Y positions and for the time of flight, MCP vs. MWPPAC.

The intrinsic time resolution of the MCP detector was measured to be 250-300 ps, and its efficiency with the heavy ions is near to 100%.

2.3.2 The Focal Plane Detectors

The focal plane detector consists of an array of Multiwire Parallel-Plate Avalanche Counters (MWPPAC) followed, downstream, by a second array of transverse field multi-parametric Ionization Chambers (IC). Fig. 2.5 shows an exploded view of the MWPPAC assembly.

The chosen detector combination is a compromise to fulfill the PRISMA requirements that can be summarized as: 1) good nuclear charge resolution for ions up to $Z \simeq 60$; 2) energy resolution $\leq 2\%$ for identifying the ion charge state; 3) fast timing ($\approx$300 ps); 4) counting rates as high as 100 kHz.

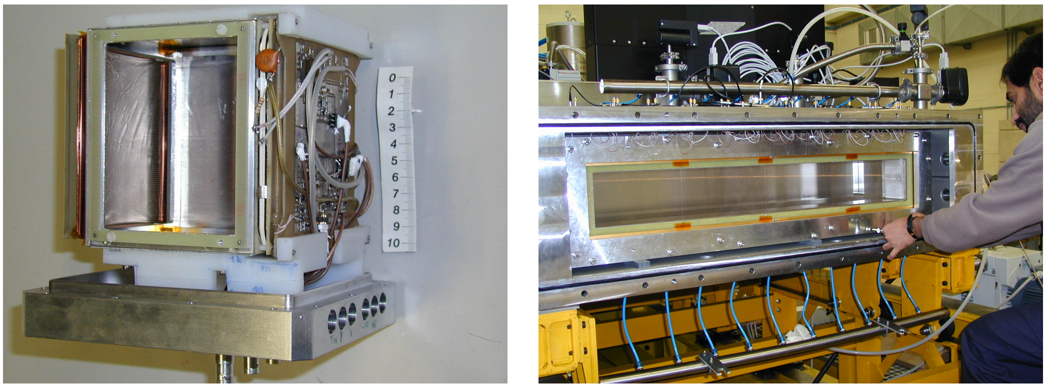

Figure 2.4: *Photos of the entrance (left) and the focal plane MWPPAC (right) detectors.*

The MWPPAC array consists of 10 equal sections for a total active focal plane surface of 100×13 cm^2. The structure is with three electrodes; a central cathode (polarized at high voltage) for timing, and X and Y wire planes for the positions, symmetrically placed, at ground potential, with respect to the cathode and at a distance of 2.4 mm from it. The X-position sensitive wires (in-plane coordinate) are distributed over 1000 mm with a step of 1 mm. Although they are divided in 10 sections of 100 wires each, there is no dead

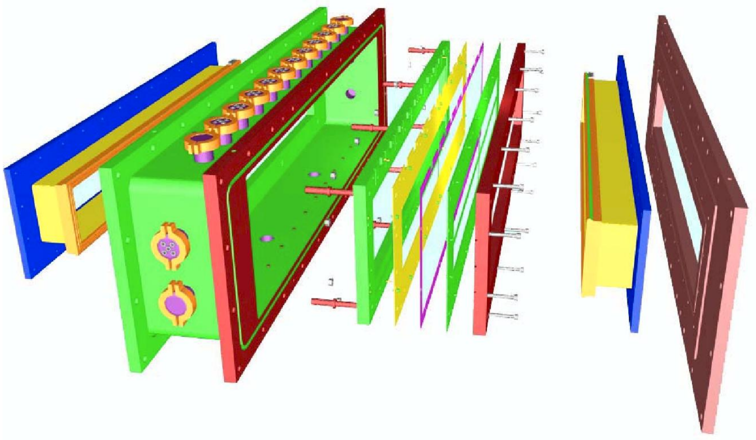

Figure 2.5: *Exploded view of the MWPPAC assembly.*

space because the sections are constructed in such a way that the 1 mm step is preserved. The position signals are derived with the delay-line method, hence one has two signals from each section, one on each side, whose relative delay is proportional to the position of the incoming ion. In order to have an attenuation of the signals as small as possible, the delay lines are produced directly on the frame where the wires are soldered. The Y position (out of plane) is made by only one section of 136 position wires over 135 mm. They are 1 meter long and the wire step is 1 mm, so to preserve the electric field symmetry. Since the required Y resolution is only 2-3 mm, they are connected in groups of two giving 68 effective position wires with a 2 mm position resolution. The choice of making the Y wires 1 m long (the full in-plane window opening) is dictated by the fact that cutting in many sections also the Y side, one would have lost $\simeq$15% of the solid angle because of the frames where the Y wires and the delay lines should have been connected.

The cathode is made by a plane of wires divided in 10 sections, like for the X wire plane. Each section constitutes one cathode with its own polarization and timing output signal. The cathode wires are mounted on the same printed circuit frame as the Y wires (on the opposite side); the same frame keeps both sets of wires. All the electrodes are mechanically connected to each other and then fixed on the vacuum vessel. Two 200 μg/cm^2 Mylar windows separate the MWPPAC gas volume from the rest of the spectrometer.

The vacuum regions upstream and downstream the MWPPAC are completely separated. Thus the region between this detector and the ionization chambers IC, where the vacuum may become poor because of the unavoidable gas leak through the IC window, is separated from the high vacuum side (upstream the MWPPAC). The possible leak on the IC side is due to the relatively high gas pressures we need (up to 100-120 mbar, CH_4 or CF_4) on a large surface Mylar window which has to be kept thin enough to preserve the energy resolution. The pressure inside the MWPPAC is in the range 7-10 mbar of Isobuthane and the gas leak through the high vacuum side window is low enough for maintaining good vacuum conditions (10^{-6}-10^{-7} mbar) at a distance of around 6.5 m upstream where the entrance MCP detector is placed.

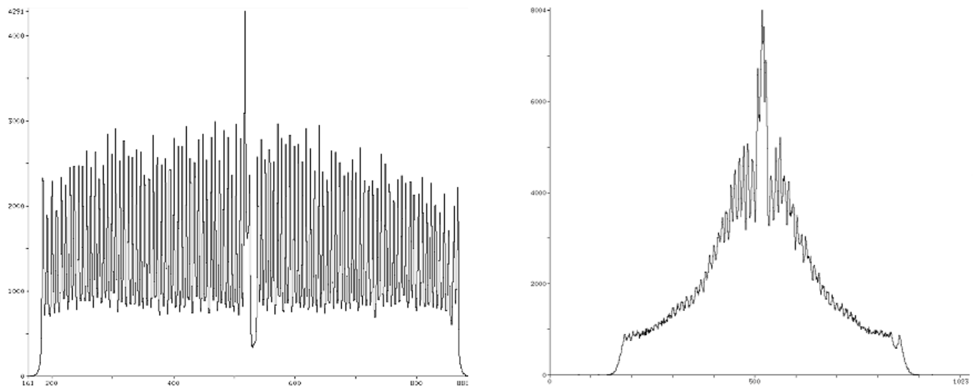

Figure 2.6: *Typical position spectra for the MWPPAC: one section of the X (left), Y (right).*

The pads of the anodes and cathodes are produced with the printed circuit technique with 2 mm isolating space between two elements. The electrical connections are made on the back side through thin metalized holes. Due to technical problems for producing such a big printed circuit, there are four equal pieces (for the anodes and for the cathodes) supported by a suitable frame. All the electrodes are mechanically connected and allocated inside the IC vessel. In addition, it is planned to install a single-wire proportional counter near the entrance window on the anode side so to allow a second measurement of the X coordinate that, combined with the X and Y positions of the MWPPAC, can give the in-plane angle of the incoming ion. A careful study has been done to produce the wire system for sustaining the Mylar foil on the IC window. In order to keep the Mylar deformation less than 3-4 mm, stainless steel wires with a diameter of 150 μm and with a step of 2 mm are used. They are stretched with 1500 g and fixed on the window frame by a special clipping system. construction.

2.3.3 The Ionization Chambers

The array of IC is at 72 cm downstream of the MWPPAC with an active full size volume of 120×13×100 cm^3 (width×height×depth respectively). The number of sections is 12 and each of them consists of 1) 4 anode elements to be used as ΔE-E in different combinations depending on the energy and type of ions under study; 2) a common Frisch grid and 3) a common cathode. Two anode sections (the leftmost and rightmost ones) are used as guard rings and vetoes for the ions going partially outside the IC active volume.

The IC covers the same total area of the MWPPAC with a 100 cm active depth and, as well as the MWPPAC, cathode and anode are divided in 10 identical sections. The depth of the chambers has chosen to be as long as 100 cm, because this length is comparable with the path length of such heavy ions, taking into account the stopping power and the maximum pressure of the gases used.

The distance between the cathode and the Frisch grid is 13 cm, and the anode is located at 13 mm from the Frisch grid. Each section of the IC is segmented in 4 equal sectors of 10×25 cm^2 providing the energy loss ΔE (for particle identification) and the total energy E. Fig. 2.7 shows an exploded view of the ionization chambers.

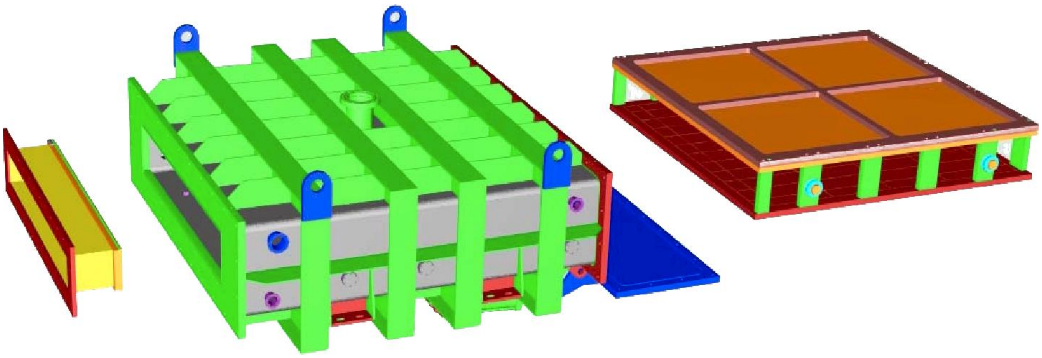

Figure 2.7: *Exploded view of the IC.*

The IC can work with different filling gases and several test have been performed: with CH_4 and CF_4. The best results have been obtained with methane (CH_4) which is a relatively fast gas but has a low stopping power with respect to CF_4. This one should be the best candidate for the filling of the detector because it is very fast (an electron drift velocity around 10 cm/μs with a reduced electric field $E/p \simeq 1.3$ V/(cm hPa) and has a higher stopping power than CH_4. However, the tests show a degradation of the energy resolution when CF_4 was used after half an hour from the filling of the detector. Then a continuous gas circulation has to be kept for a long-term stability of the detector operation.

The IC has been tested with methane at pressures ranging from 20 to 40 hPa. The working pressure, depending on the reaction, must be adjusted to a value such that the maximum range of the fragments produced in the reaction almost equals the chamber length (1 m). The cathode was held at ground potential while the Frisch grid and the anodes were biased at 200 V (400 V) and 400 V (800 V) respectively, corresponding to a reduced electric field (E/p) of about 0.8 V/(cm hPa) in the active region. See Fig. 2.8.

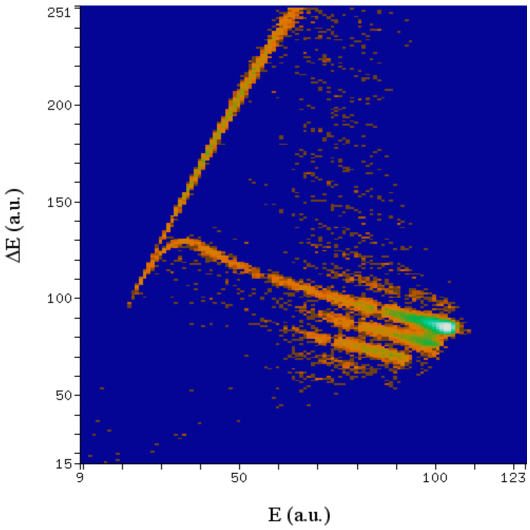

Figure 2.8: *A typical energy loss vs. total energy scatter plot, measured in the PRISMA ionization chambers for the reaction* ^{32}S+^{208}Pb, $\theta_{\rm lab} = 80^o$, *at 195 MeV.*

Chapter 3

Data Acquisition on PRISMA

During a run, the data are taken on-line from the detectors by a farm of computers and written on magnetic tape or hard disks for final analysis. PRISMA generates an average trigger rate of 10 kilo-events per second, with peaks of 100 kilo-events per second depending on the entrance angle, the reaction participants, the energy, and so on...

The PRISMA data acquisition system is an application of the "General Framework for Small Acquisition Systems" [5] that has been designed at LNL, in the last years, to face up the data acquisition requirements for potentially any type of experimental setup. Up to now, it has been successfully used with GASP, PRISMA and the test-beam for CMS. This acquisition framework, quite general and flexible, was initially developed for the Sun workstations on the basis of the Euroball acquisition system. The experience with PRISMA drove to a complete porting of the whole system to the more convenient and modern Linux environment, running on common desktop computers. The porting led also to a deep re-design, renewal and rewriting of the existing software which are also object of this thesis. The PRISMA Data Acquisition framework was also enriched with several tools designed specially for PRISMA and for the experiments performed at LNL; these tools will be described in this chapter.

3.1 Overview of the DAQ System

The acquisition scheme is shown in Fig. 3.2. About hundred electronic channels come out from the PRISMA detectors. All these signals are handled by a single VME crate which, through a PCI/VME interface, sends the data to a farm of Linux computers. The acquisition software, running distributed on the farm, takes care of collecting, histogramming and displaying the data, and gives the user the possibility to interact with the data and to perform on-line analysis (see Fig. 3.1).

The Data Acquisition System for the combined PRISMA-CLARA set-up has to collect the data generated at high event rates. The corresponding raw data rate depends on the particular experiment and rates up to 4 MB/sec with 200 electronic channels have to be handled by the system. To combine the two sub-systems and to accomplish the requirements, a DAQ design was developed on the base of event synchronization with a time stamp technique.

The acquisition system has been developed in collaboration between the LNL and Daresbury data acquisition groups using as a base the Euroball distributed system. The VXI electronics setup and control, and most of the starting procedures for the front end electronics are done through the MIDAS software [29]. The user graphic interface (OCP) for the distributed acquisition system has been programmed at LNL and allows an easy interaction of the users with the system.

The data merging procedure is based on the synchronization VME card TITRIS developed at GSI Darmstadt. The necessary tools have been programmed by the LNL data acquisition group, and are fully compatible with the present LNL Linux version of the NEO++ software [33]. Since the setup does not include VXI Euroball trigger cards, it has been necessary to design and build a trigger interface for the VXI electronics. The module, developed at INFN-Padua, includes all inputs and outputs of the trigger, validation and inhibit signals. Work on the HV power supply control system is still in progress at LNL. The shutdown hardware is already working for protection, in connection with the cryogenic control system. The PRISMA-CLARA Data

Acquisition System structure is shown in Fig. 3.2. The main components are the Readout Unit (RU), the Builder Unit (BU) and the Filter Unit (FU). The purpose of the Readout Unit is to read events from the front-end electronic, buffer them locally and serve them to the Builder Unit. The Filter Unit are "spy" channels on which events can be redirected for the feeding of the lower level analysis programs or monitoring systems, without interfere with the data flux directed to the mass storage devices.

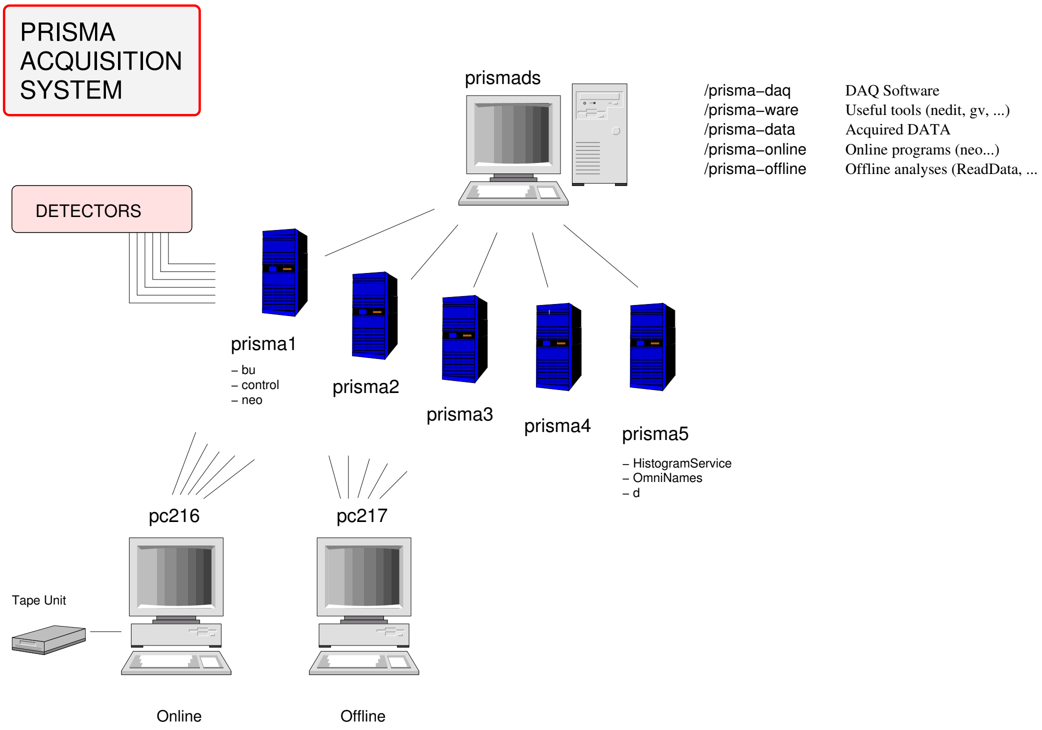

Figure 3.1: *Scheme of the computer farm used for the data acquisition.*

3.1.1 Electronics and Readout

The PRISMA data acquisition system is based on the VME bus (CAEN modules): one 32 channels TDC (V775); three peak-sensing 32 channels ADC (V875); and a 32 channels scaler (V830). All these modules are read-out by a VME CPU.The CPU contains a trigger card with a readout input signal and the busy and veto outputs for the trigger electronics. This CPU sends the information to a farm of Linux PC (see Fig. 3.1) which acts as event builder and processing farm. The farm is connected through the acquisition network (through an Ethernet connection) to the histogram server, tape server and disk server. In addition, it is possible to use extra Linux computer as spy processors for the on-line analysis. The farm of event builders and the spies are programmed in C++ extended by the NEO++ library.

3.1.2 NEO++ Event Formatter

To cope with the complexity of the analysis programs for nuclear physics experiments, powerful programming language constructs have been made available to the users. Central to analysis programs is the concept of “event”, i.e. a collection of digitized data corresponding to a signal produces by a detector in the spectrometer. The event is set up both from the input data source and the basic unit of elaboration in on-line and (possibly) off-line programs. For these reasons it seems natural to express the idea of event in a programming language by means of reserved keywords or dedicated features. In order to do that, a battery of C++ classes and macros has been created, extending the basic set of keywords of such programming language; this gives the user the possibility to handle the events in a high level programming environment. The set of libraries was called “NEO++”. An example of simple acquisition program, written in NEO++, is presented in the Appendix.

3.1.3 On-line Data Histogramming

The raw data histogramming is required to offer high speed of response and stability, and to guarantee the success of the acquisition process and of the experiments. For this reason, the system of histogramming has been developed as a distributed application on a dedicated computer farm, so that accidental crashes of the histogramming system would not affect other, more important, jobs, such as the data taking and the data storage. The choice

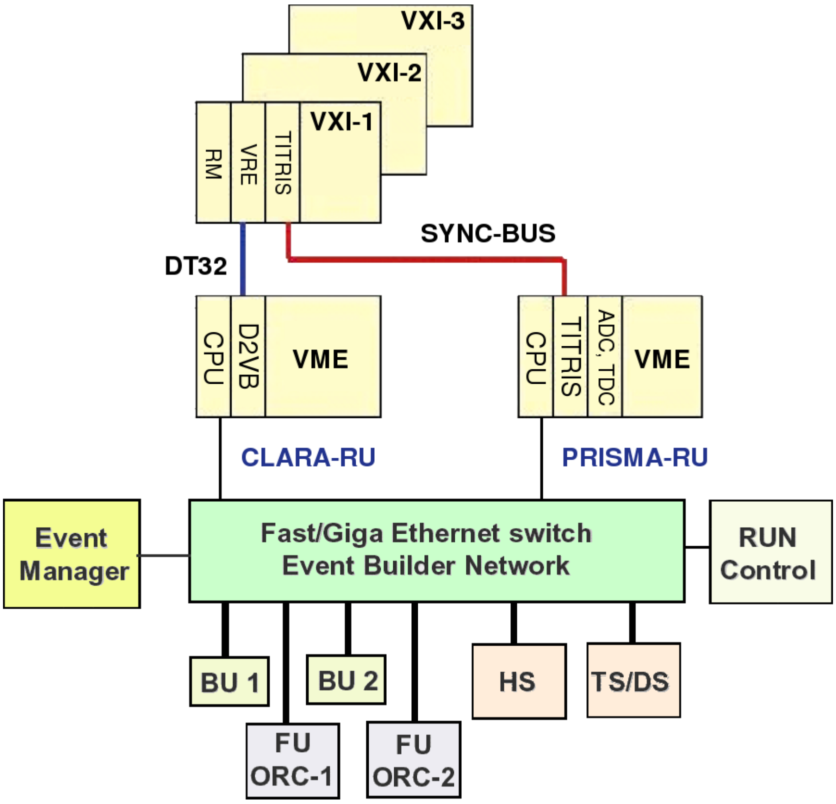

Figure 3.2: *Block Diagram of the PRISMA-CLARA Data Acquisition system.*

for the computer farm has also been necessary in order to face up the high trigger rate of PRISMA and the large number of signals acquired (for example, when coupled with the CLARA array of germanium detectors, the total number of signals grows up to about two hundreds).

The architecture of the system has been based on the client(s)/server paradigms. When an acquisition process boots up, it contacts the histogram server, which is running on a dedicated machine. At this moment, the histogram server scans a list of the computers in the farm and selects the one with the lowest CPU load. Then, the server connects the acquisition programs with the histogramming process and let them communicate directly with each other.

The communication protocol between the acquisition processes and the histogram server, and between the histogramming programs and the server is based on the CORBA technology for distributed applications, while the communications between the acquisition processes and the histogramming programs are direct implementations of the TCP/IP protocol.

3.1.4 On-line Data Displaying

During the data taking, single spectra of entrance position, focal plane position, time of flight, ΔE and E, two-dimensional spectra of entrance x vs entrance y, focal plane X vs time of flight, ΔE vs E, or any other user-defined histogram, are accumulated and can be individually displayed on the computer screen. A tool for displaying the histograms has been created, called `d`. The `d` program was originally created for the PISOLO spectrometer, and has been adapted to the PRISMA case by introducing the communication protocols required by the distributed histogramming service.

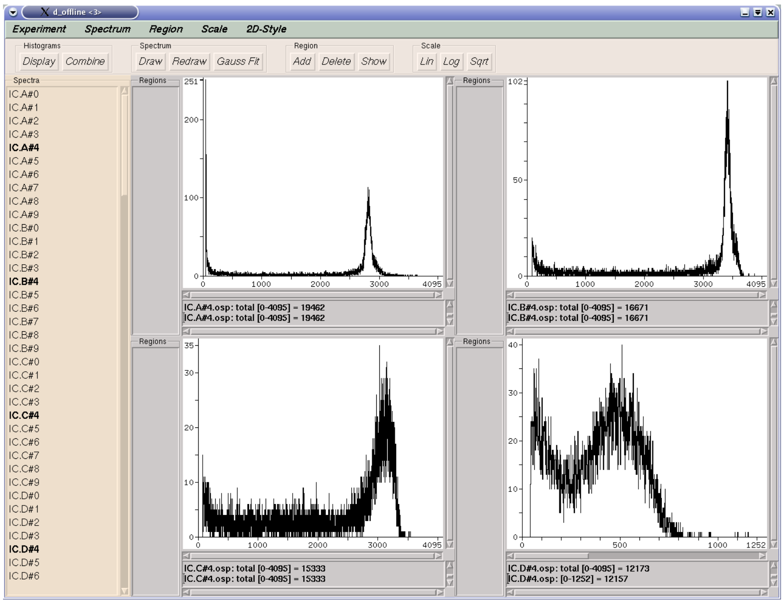

```
IC.A#4.osp: total [0-4095] = 19462
IC.A#4.osp: total [0-4095] = 19462
```

```
IC.B#4.osp: total [0-4095] = 16671
IC.B#4.osp: total [0-4095] = 16671
```

```
IC.C#4.osp: total [0-4095] = 15333
IC.C#4.osp: total [0-4095] = 15333
```

```
IC.D#4.osp: total [0-4095] = 12173
IC.D#4.osp: [0-1252] = 12157
```

Figure 3.3: *A screenshot of the histograms display,* `d`*, here showing the energy spectra of four sections of the ionization chambers.*

3.1.5 On-line Data Storage

The interface provided to the final user allows to manage a tape like an object in the system and then to perform read-write operations of fixed sized buffers over it. Transparent to the user is the effective device location and set-up: it is performed through a graphical interface; it provides the association of one or more devices to the object defined in the program and a "manager" program enables/disables the operations issued by the analysis processes.

The media used for the data storage are magnetic tapes and hard discs. Usually both the systems are in use at the same time. The disc storage allows quick data sorting, so that the user can perform preliminary off-line analysis of part of the data, even during the on-line data taking. The disc system of PRISMA consists in a disc server, equipped with 5 Tb of disc space. The tape units (DLT technology) are used for back-up purposes. The average amount of acquired data per experiment is about 200 GB, depending from the experimental conditions and the reaction in study (trigger rate, detecting angle, etc.).

3.1.6 On-line Data Monitoring: Spy Channels

One of the PRISMA system requirements stresses the fact that the farm of computers dedicated to event processing should be divided in (at least) two levels: in the upper one a certain number of computers should be dedicated essentially to events reassembling, formatting and mass-storage recording, while in the lower one a real complex analysis should be possible on (at least a part of) the event flow. A link between the two levels should be explicitly provided inside the data acquisition program. For this purpose, the PRISMA acquisition software includes the definition of so-called "spy" channels on which events should be redirected for the feeding of the lower level analysis programs. From the user perspective, spy channels are semantically equivalent to mass storage output channels, terminal output channels,. . . : in other words, all of them are treated as generic output streams.

3.2 Overview of the Experimental Histograms

This section is an overview of the plots which are important during an experiment or an analysis. In spite of the complexity of the spectrometer, which provides hundreds of signals, a few on-line raw spectra and matrices involve a clear and direct physical interpretation. The experimentalist must be aware of this in order to face up the experimental needs and to tune the instrument.

3.2.1 Entrance Position Detector

The entrance detector provides an X and Y two-dimensional spectrum. A typical example is shown in Fig. 3.4. This spectrum has been obtained during an experiment, when the trigger of the acquisition system was set as a logic "AND" between the signals of the MCP and the PPAC detectors, so that only the events passing through the MCP and also reaching the PPAC were triggering the start of the acquisition process. Observing this matrix, three characteristics are clearly visible: (1) the elliptic shape of the highlighted part, (2) a cross with four arms within it, and (3) a slight background surrounding the ellipse. The elliptic shape of the matrix is easily understandable considering the geometry of PRISMA: since the detecting surface of the Micro Channel Plate is placed between the target and the quadrupole entrance, the fraction of the reaction products emitted at the target's point, that the spectrometer transmits toward the focal plane, is approximately a cone entering the quadrupole and crossing the MCP. The ellipse raises from the intersection between this cone and the detecting surface of the MCP.

The cross visible in the figure is the projection of a mask placed on the Carbon foil and it is used for calibration purposes. This mask has four arms intersecting in a point which is almost coinciding with the center of the MCP, namely the point where the central trajectory of PRISMA crosses the carbon foil. Four small flags are visible on the cross arms. These flags are 4 cm distant from the center and are used for calibration purposes. All this information allows the user to calculate the entrance angles (θ, ϕ) of the ions traversing

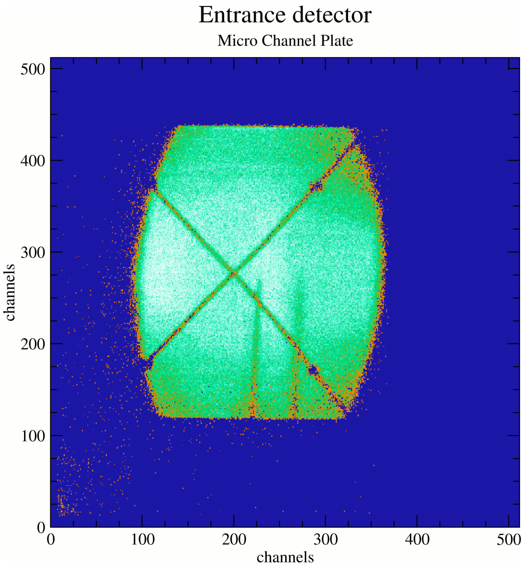

Figure 3.4: *Typical two-dimensional histogram of the entrance detector. Every pair* (X, Y) *in the matrix corresponds to a bin, whose color relates the number of counts it is carrying in. Here and in the following colored scatter plots, the blue indicates an empty bin (zero counts), whereas the colors, shading to the white, correspond to the bin which are populated.*

the PRISMA.

3.2.2 X-TOF Matrix at the Focal Plane Detectors

By gating on the MCP detector's $X - Y$ matrix (i.e. by reducing the entrance solid angle of PRISMA), an histogram showing the horizontal position on the focal plane X versus the time of flight TOF looks like Fig. 3.5. The structures visible in this matrix are related to the specific characteristics of the ions detected by the spectrometer (such as mass, charge, velocity, etc.). In order to understand this matrix, we need considering the equation governing an ideal spectrometer:

$$B\,\rho = \frac{p}{q}. \tag{3.1}$$

The quantity $B\,\rho$ is called *magnetic rigidity* and addresses the resistance opposed by the particles to the bending of their trajectories due to the magnetic field B; ions with a higher magnetic rigidity will be deflected less than ions with a lower magnetic rigidity. For this reason, we can roughly say [37] that the position of the focal plane is related with the magnetic rigidity of the ions,

$$B\,\rho \sim X. \tag{3.2}$$

X denotes the horizontal position of the ions on the focal plane; in other words, higher rigidities mean less deflection, which implies larger X positions on the focal plane, whereas lower rigidities mean higher deflections, i.e., smaller X positions on the focal plane. The vertical axis, TOF, shows the time of flight information, expressed in channels (here 10 channels correspond to 1 ns). Notice that, since the TOF is measured from the time occurring between a start signal, generated by the focal plane detector, and a stop signal, generated by the entrance detector (suitably delayed), the time of flight grows downwards.

Let us now examine the structures visible in Fig. 3.5. Equations 3.1 and 3.2 relate the ions ionic charge state q with the magnetic rigidity; in other words, magnetic spectrometers deflect different ionic charge states q to different positions X of the focal plane, according with the inverse of their charge state q; namely, higher charge states are deflected more (right side of the picture), while lower charge states are deflected less (left side of the picture). Usually, the intensity of the magnetic field of the dipole is calculated so that the mean charge state q is placed at the center of the focal plane. Referring to Fig. 3.5, i.e. the reaction ^{90}Zr+^{208}Pb at 560 MeV, the central charge state was $q = 33^{+}$. In this picture 6 different charge states, from $q = 31^{+}$ to $q = 36^{+}$, are visible.

Looking at this matrix, it emerges that the events are clustered in structures shaped like bands. What is the physical meaning of these structures? It is possible to understand it, selecting a narrow vertical slice on the graph and reminding equation 3.2. Selecting vertically on the X-TOF matrix, namely

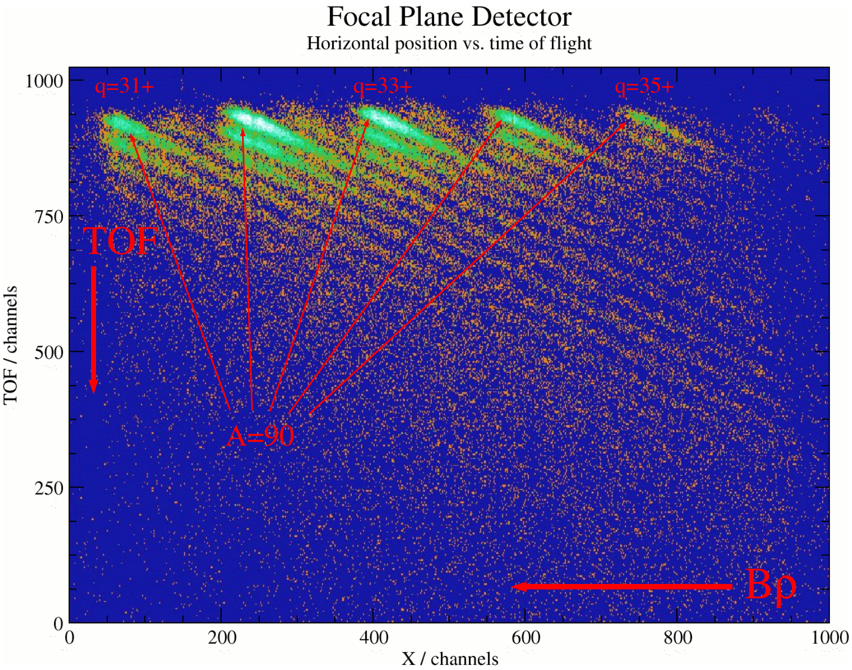

Figure 3.5: *Horizontal position on the focal plane, X, vs. time of flight, TOF, for the reaction ^{90}Zr+^{208}Pb at 560 MeV. The X axis shows the whole X focal plane of PRISMA, which is 1 meter large. The X axis grows from left to right as if it is seen from the beam view.*

corresponds to pick a constant $B\rho$ and neglect the superimposition of the ionic charges states, focusing only on a particular charge state q. Therefore, according to equation 3.2, when two events have the same charge state and magnetic rigidity, but different TOF, they must have different momenta. Particles having different momenta $p = mv$, must have either different velocity or different mass. Therefore the different bands correspond to different masses. Since heavier masses correspond to slower ions (i.e. longer time of flight), this means that the mass number grow in the same direction of the TOF, downwards.

3.2.3 Ionization Chambers

When an ion in a certain charge state, e.g. a reaction product, passes through a gas detector, it ionizes the gas molecules. If the gas detector operates as an ionization chamber or in the proportional regime, the integrated charge is proportional to the energy loss, which itself depends on the charge state, the mass and the energy of the ion. The rate of energy loss of an ion passing through a medium is described by the well-known Bethe-Bloch equation [17]. For non relativistic particles, one has approximately

$$\frac{dE}{dx} \propto \frac{M\, Z_{eff}^2}{E} \tag{3.3}$$

where dE is the energy loss over the differential distance dx, M is the atomic mass and Z_{eff} is the effective nuclear charge state of the ion.

Equation 3.3 suggests the use of a detector system consisting of a gas-detector, which measures the energy loss ΔE over a small distance Δx with

$$\Delta E \equiv \frac{dE}{dx}\Delta x \tag{3.4}$$

followed by a measurement of the residual energy E_{res}. The sum of ΔE and E_{res} gives the particle's energy E. The product $E\,\Delta E/dx$ provides a measure of $M\,Z^2$ in this simplified case. In a plot of ΔE versus E, different charge states correspond to segments of hyperbolas which have their vertexes at different points of the diagonal $\Delta E = E$. These segments of hyperbolas identify different Z lines.

Lengthwise, the forty ionization chambers of PRISMA are divided in four rows composed by ten sections each one. The energy measured in the first (or first two) row(s) of the ionization chambers act as ΔE, while the total energy released inside the whole chambers is the E. In Fig. 3.6, ΔE and E are plotted on the vertical and on the horizontal axes, respectively. In this plot, the most evident line is due to the beam-like ions (such as the elastically scattered ones, for instance), because of their larger cross section; proton pick-up and proton stripping appear respectively above and below this line; so that the atomic number Z grows upwards.

It must be noticed, however, that for the heaviest elements some overlap exists. The intrinsic limits to the energy resolution of these gas filled detectors, approximatively $\Delta E/E \simeq 1.5\%$, contitute a contraint that must be taken into account.

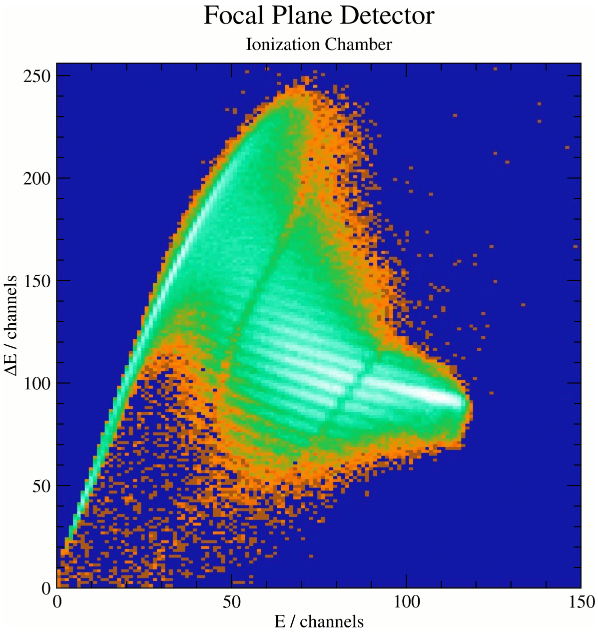

Figure 3.6: *Energy released in the first row of the ionization chambers, ΔE, versus total energy E of the ions, for the reaction ^{82}Se+^{238}U at 505 MeV. In this matrix several Z lines are clearly visible. The beam-like particles correspond to the highlighted line. Proton stripping and proton pick-up are respectively below and above this line.*

Chapter 4

Particle Identification on PRISMA

4.1 Strategy

The identification of the reaction products on PRISMA is based on the reconstruction of the ion trajectories. The strategy proposed at this purpose consists in two steps: a preliminary geometrical approximation for the central trajectories, where the simple behavior of the magnetic fields is exploited in order to obtain an absolute calibration of the TOF raw signals, then, the full tracking of the ion paths event by event. The core of the tracking code consists in three parts, an integrator of the equations of the motion, an accurate model of the magnetic fields and a minimization procedure, for minimizing a merit function quantifying the agreement between the on-line and the simulated signals.

4.2 Geometrical Trajectory Reconstruction

The TOF raw signals need to be calibrated in order to provide a reliable time information in unit of nanoseconds, instead of channels. This is required by the tracking algorithms.

By virtue of the equation

$$B\rho = \frac{p}{q},$$

$$\frac{p}{q} = \frac{m\,v}{q} = \frac{m}{q}\,\frac{S}{TOF}$$

one obtains

$$TOF = S\,\frac{m}{q}\,\frac{1}{B\rho}.$$

Therefore, if one knows m/q ratio (it can be taken from the X-TOF matrix), pathlength, and radius of curvature ρ, it is possible to calculate the absolute TOF.

To a first approximation, the path length and the radius can be calculated geometrically, at least for certain trajectories. The trajectories close to the central one, for example, can be decomposed in elementary parts such as two straight lines and a circular sector, because the quadrupole field vanishes along the central axis and the dipole field can be reasonably considered constant. Therefore, any central trajectory is composed in three parts: (1) a straight line, connecting the target with the entrance of the dipole, (2) a circular sector, when the ion passes inside the dipole, and again a straight line (3), when the ion flies in the vacuum, from the dipole exit until the focal plane is reached.

The calculation of the trajectory length

$$L = L_{MCP} + L_{DIPOLE} + L_{PPAC},$$

starts from the focal plane and entrance detectors and proceeds along straight lines toward the dipole magnet, where the radius of curvature is calculated from geometrical information. The algorithm is summarized as follows:

1. computation of the entrance angle at the PPAC, by means of the position information provided by the IC and by the PPAC itself. It is worth to remember that the ionization chambers IC are composed by 4 rows, each divided in 10 sectors, which correspond to the 10 sections of the PPAC. The IC do not really give a position information, but

it is possible to calculate it considering the relative amount of energy released by an ion in each section.
There are two possible cases: 1) the trajectory is oblique and the ion crosses consecutive sections of several rows, 2) the ion proceeds perpendicularly to the detector. In the first case, the ion releases part of its energy in each one of the triggering sections and we can calculate its position by an average weighted by the energy released in each one of them:

$$X = \frac{\sum_{[i]} X_{[i]} \cdot \Delta E_{[i]}}{\sum_{[i]} \Delta E_{[i]}},$$

where $[i]$ tags the IC section and runs from 0 to 9. See Fig. 4.1. In the second case the ions likely "fires" only one section per row; this is the worst case, since it is not possible to guess the ion position better than assuming it is passed through the middle point of the triggering section.

2. back projection of the trajectory from the PPAC to the dipole exit (this gives the base of the tangent vector to the trajectory, at the dipole exit, whose direction has been calculated at (1)). Assuming a system of reference located at the dipole exit, with the X axis along the effective field boundary of the dipole, the Y axis directed toward the focal plane detectors and the Z axis perpendicular to the focal plane (see Fig 4.2), the desired projection is

   $$\vec{q} = \vec{q} - \hat{m} \cdot \frac{q_y}{m_y},$$

   where $\vec{Q}$ is the vector position of the ion, and $\hat{m}$ is the tangent unit vector to the trajectory, that is $\hat{m} = \frac{\vec{q}}{|\vec{q}|}$;

3. computation of the position of the ion at the dipole entrance. For ions directed along the central trajectories, this information is straightforwardly evaluable. Since the quadrupole field can be neglected along its axis, this distance derives only from the set-up geometry and, in particular, from the distance between the MCP and the dipole entrance

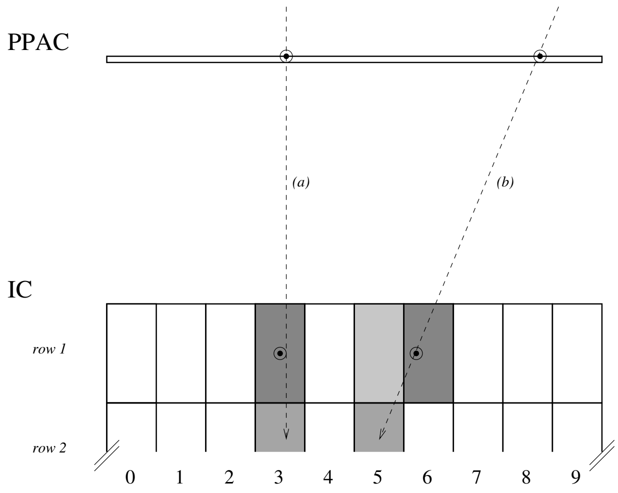

Figure 4.1: *Extracting the position from the ionization chambers. (a) When a particle enters straightly the detector, we barely assume it passed through the middle point of the triggering section. (b) When the trajectory is oblique, the position is calculated as an energy-weighted average of the positions of the triggering sections. In the picture, different tones of gray represent different amounts of energy released in the section (darker=more energy). We finally calculate the ion's direction combining this information with the position provided by the PPAC.*

window, i.e.

$$L_{MCP} = (160 - 25)\ \text{cm} = 135\ \text{cm}.$$

4. computation of the curvature radius R of the trajectory, inside the dipole, fulfilling the conditions imposed by the previous steps on the tangents to the direction at the entrance and exit of the dipole. Assuming $\vec{P}$ and $\vec{Q}$ as representing the ion position at the entrance and at the exit of the dipole, respectively, and $\hat{m}$ and $\hat{n}$ being the unit vectors tangent to the trajectory, respectively in $\vec{P}$ and $\vec{Q}$ (see Fig. (4.4)). The vector connecting $\vec{P}$ and $\vec{Q}$, barely $\vec{PQ} = \vec{Q} - \vec{P}$, is a chord of the circle subtending the arc whose length we are now calculating (see Fig. 4.4). Identifying with $\vec{C}$ the center of this circle, we know from trigonometry

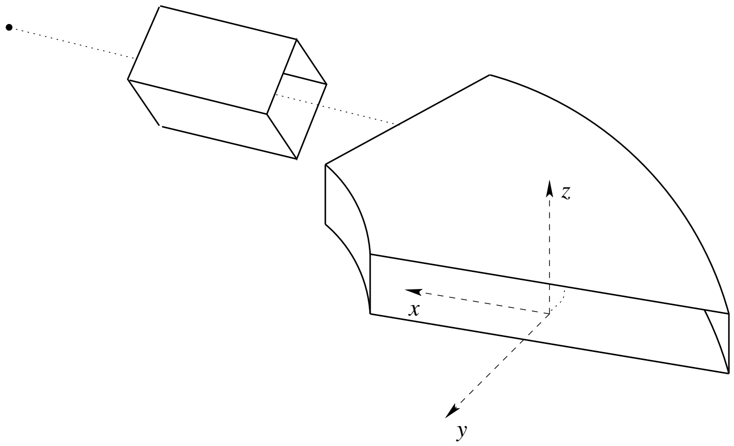

Figure 4.2: *System of reference system used when calculating the position of the ions at the exit of the dipole. It refers to the effective boundary of the dipole magnetic field.*

that:

$$R = \frac{|\vec{Q}-\vec{P}|}{\cos(\frac{\Pi}{2}-\alpha)} = \frac{|\vec{Q}-\vec{P}|}{\sin(\alpha)},$$

where α is the angle between $\hat{m}$ and the vector $\vec{Q}-\vec{P}$,

$$\alpha = \arccos\left(\hat{m} \times \frac{\vec{Q}-\vec{P}}{|\vec{Q}-\vec{P}|}\right).$$

The length of this part of trajectory, L, follows now straightforward:

$$L_{DIPOLE} = 2 \cdot \alpha \cdot R = 2 \cdot \alpha \cdot \frac{|\vec{PQ}|}{\sin(\alpha)}.$$

In order to evaluate the reliability of the algorithm, this approximation has been applied to simulated trajectories and compared with the corresponding real pathlengths. Three cases have been examined: trajectories covering the full entrance angle of PRISMA, trajectories belonging the dispersion plane and central trajectories[1].

---

[1] For this computation the approximation was extended in order to take into account the effects of the quadrupole, in a rough approximation.

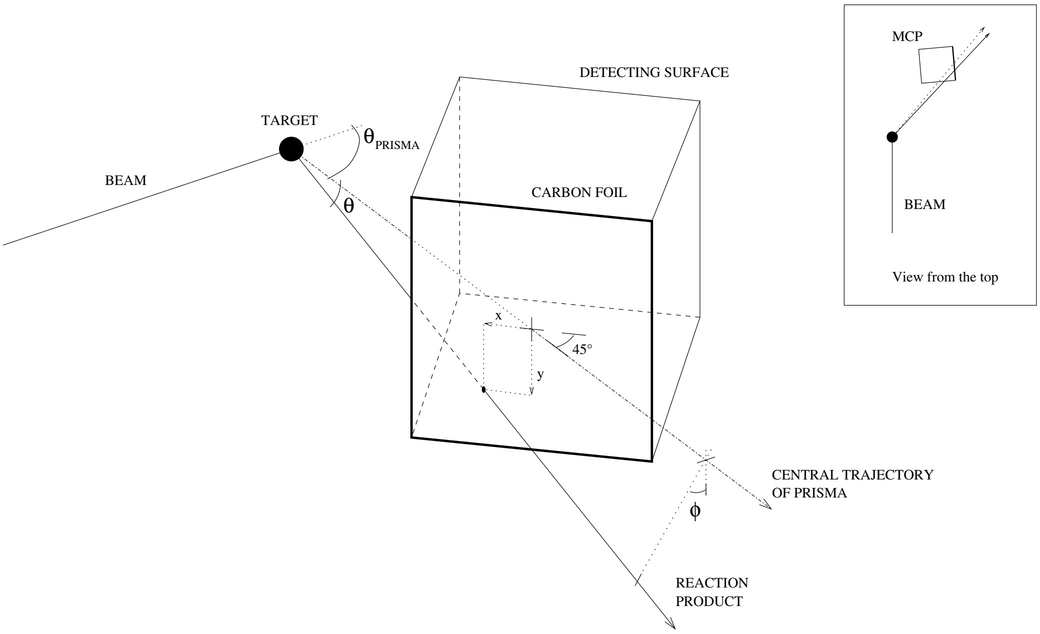

Figure 4.3: *System of reference used on the entrance detector. The reference frame for the* MCP_x *and* MCP_y *signals is located in the center of the carbon foil, as illustrated in the figure. The ion direction is determined by the polar angles* (θ, ϕ) *shown in the picture.*

An event generator, simulating Rutherford scattering events, has been used. The simulated reaction was ^{56}Fe+^{197}Au at 186 MeV in the laboratory's frame, which is in fact an energy below the Coulomb barrier. Fig. 4.5 depicts the histograms of the ratio between the simulated trajectory length and its approximation on 100000 events for each one of the three cases.

Fig. 4.5 shows the good reliability of the geometrical approximation for the central trajectories, and reveals its inaccuracy in the other cases. Let us examine, from the plot, the average ratio r, defined as

$$R =< R > \pm \sigma_R,$$

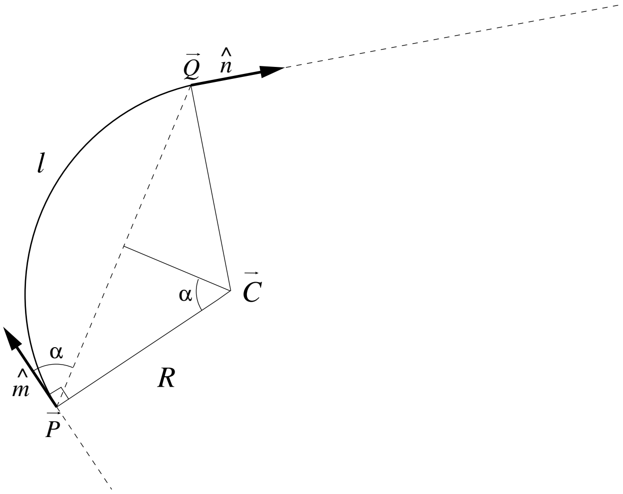

Figure 4.4: *The notations used calculating the length of the trajectory inside the dipole. The ion enters the dipole in $\vec{P}$ and gets out in $\vec{Q}$.*

for each case:

$$\begin{aligned} R_{full} &= 0.997 \pm 0.024 \\ R_{planar} &= 0.999 \pm 0.021 \\ R_{central} &= 0.999 \pm 0.002 \end{aligned}$$

As it will be shown in the following sections, the mass identification depends strongly on the quality of the q charge state identification. The resolution $\Delta q/q$ in charge state identification depends itself from the path length. From

$$q = \frac{2}{S(\theta,\phi)} \cdot \frac{E \cdot TOF}{B\rho(\theta,\phi)},$$

where E is the total energy, TOF is the flight time and $B\rho(\theta,\phi)$ is the magnetic rigidity, derives that the errors of these values propagate to $\Delta q/q$ like this:

$$\frac{\Delta q}{q} \simeq \sqrt{\left(\frac{\Delta S}{S}\right)^2 + \left(\frac{\Delta TOF}{TOF}\right)^2 + \left(\frac{\Delta E}{E}\right)^2},$$

where

$$\frac{\Delta S}{S} \simeq \frac{\Delta R}{R}.$$

For the three cases:

$$\frac{\Delta R_{full}}{R_{full}} = 2.4\% \tag{4.1}$$

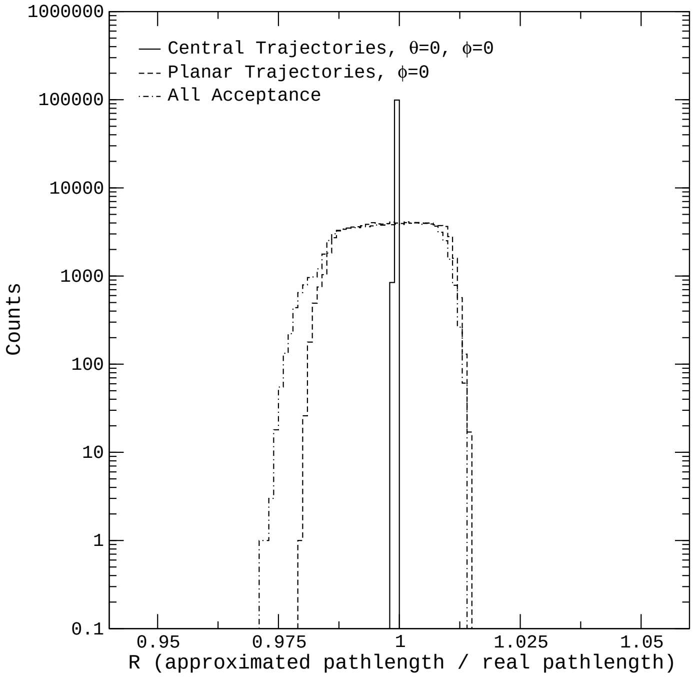

Figure 4.5: *Monte Carlo simulations showing the histograms of the ration between the length of 100'000 realistic trajectories (i.e. calculated taking into account the correct dipole and quadrupole fringe fields) and their approximated length (calculated with the algorithm described in the text). Continuous line: central events; Dashed line: events belonging to the dispersion plane; Dashed and dotted line: all solid angle.*

$$\frac{\Delta R_{planar}}{R_{planar}} = 2.1\% \qquad (4.2)$$

$$\frac{\Delta R_{central}}{R_{central}} = 0.2\% \qquad (4.3)$$

Therefore, the approximation for central trajectory is quite reliable, whereas it fails for the other trajectories (this implies that full tracking algorithms are specifically required).

The need for an accurate ion trajectory reconstruction rises also from another reason. The heart of this approximated method lies in the geometrical issues of the problem, but, actually, we must consider also that the position information obtained from the ionization chambers is very poor.

4.3 Ray Tracking

The off-line analysis, being (to some extent) unaffected by the speed constraints of the high frequency rates of the on-line data taking, allows the user to apply more accurate data analysis algorithms and sophisticate techniques, which, in the specific case, must involve the full ion tracking inside the spectrometer. We stress here that tracking the ions means calculating the length of the trajectories, and that this implies considering properly the magnetic fields of the PRISMA. In order to perform this computation, an ion tracking code has been developed. This code has been written in the C++ programming language.

The ion track integrator appears to the user like a black box: it takes an input describing the experimental conditions, then, event by event, calculates the trajectory, transporting the ions up to the focal plane. It provides, as output, the ion position on the PPAC, the TOF and the the length of the trajectory. The parameters related to the spectrometer, such as its central angle, the magnetic field intensities must be provided by the user before to start the analysis.

An ion is fully identified when its mass m, its charge states q and Z, and its energy E are known. As it is shown in the previous chapters, we can get some of these quantities directly from the raw signals we take out from the detectors after their calibration, that is:

- the entrance direction in the spectrometer, (θ, ϕ);
- an estimate of the m/q ratio, from the $X - TOF$ matrix;
- the identification of the Z, from the $\Delta E/E$ matrix;
- the position on the focal plane;

- the time of flight TOF (made absolute, as it will be described in the following sections.).

The charge state q identification will be described in the next chapter. When the charge state q is know, the mass is identified.

The algorithm searches for the parameters that match the experimental data, among all possible trajectories reaching the focal plane in the point $(X_{[E]}, Y_{[E]})$ with the $TOF_{[e]}$. It works as follows:

1. initialize the simulation engine;
2. initialize a candidate particle, setting up the estimated m/q ratio, the initial direction taken from the MCP and the approximative energy (taken from the ionization chambers);
3. transport the particle up to the PPAC and calculate the quantity:

   $$\chi^2 = (TOF_{[s]} - TOF_{[e]})^2 + (X_{[s]} - X_{[e]})^2 + \ [\ (Y_{[s]} - Y_{[e]})^2\ ]\ ,$$

   where $X_{[s]}/Y_{[s]}$ and $X_{[e]}/Y_{[e]}$ are the ion's horizontal/vertical positions on the focal plane, respectively simulated $(X_{[s]}, Y_{[s]})$ and estimated $(X_{[e]}, Y_{[e]})$, and, analogously, $TOF_{[s]}$ and $TOF_{[e]}$ are the simulated and the estimated TOF;
4. change suitably m/q, the velocity v and go back to item number 2, until the minimum of χ^2 is found [15].

4.4 Numerical Ion Optics

The strength of the identification procedure relies in the suitable and reliable simulation of the magnetic fields and their fringing fields.

There are several codes for simulating particle optical systems. Generically, those codes fall into two categories. One category includes ray tracing codes, which use numerical integrators to determine the trajectories of individual rays through external and possibly internal electromagnetic fields. The core of such a code is quite robust, flexible and accurate; but its execution may be somewhat slow.

The other category of codes are the map codes, which compute Taylor expansions to describe the action of the system on the phase space. Describing the field configuration through a chain of transport matrices, these codes are usually faster than the integration ones. On the other hand, traditional mapping codes have only very limited libraries for quite standardized external fields and lack the flexibility of the numerical integration techniques. In particular, only integration codes can treat properly the fringe fields.

With the magnetic spectrometer PRISMA, the accurate simulation of the fringe fields is crucial. The correct working of the spectrometer, in fact, depends also on the software for analysis, which must reconstruct the ion trajectories, event by event, taking into account the magnetic fields with their correct fringe fields. The simulation of the magnetic fields has been realized by means of the Finite Element Method [7].

4.4.1 Magnetic field Computation

In the static form the Maxwell's equations, in regions without charges or currents, have the form

$$\nabla \cdot E = 0, \quad \nabla \times E = 0, \tag{4.4}$$

$$\nabla \cdot B = 0, \quad \nabla \times B = 0. \tag{4.5}$$

As it is known, the electrostatic potential is determined by the second-order differential equation, the Laplace equation, $\nabla^2 \phi = 0$. In this case, the magnetic field can be determined from the same equation by defining a new quantity, the magnetic potential U_m such that

$$\nabla^2 U_m = 0. \tag{4.6}$$

Equation 4.6 is formally equal to the Laplace equation. This means that methods used for electric field problems, in source-free regions, can also be

applied to determine magnetic fields[2].
Examples of a numerical method for solving the Laplace equation are discussed in the following sections. The final calculations of the magnetic fields are a direct solution of the intermediary of the vector potential. The numerical technique of successive over-relaxation is explained and emphasized.

The main reason for using the Laplace equation, rather than solving for magnetic field directly, is that boundary conditions can be satisfied more easily. The difficulty, in solving the Maxwell equations directly, lies in determining boundary conditions for vector fields on surrounding conducting surfaces.

Numerical Solutions to the Laplace equation

The Laplace equation determines electrostatic potential as a function of position. Resulting electric fields can then be used to calculate particle orbits. Electrostatic problems may involve complex geometries with surfaces at many different potentials. In this case, numerical methods of analysis are essential. Digital computers handle discrete quantities, so the Laplace equation must be converted from a continuous differential equation to a finite difference formulation. As shown in Fig. 4.6, the quantity $\Phi(i,j,k)$ is defined at discrete points in space. These points constitute a three-dimensional mesh. For simplicity, the mesh spacing Δ between points in the three Cartesian directions is assumed uniform. The quantity Φ has the property that it equals $\phi(x,y,z)$ at the mesh points. If ϕ is a smoothly varying function, then a linear interpolation of Φ gives a good approximation for ϕ at any point in space. In summary, Φ is a mathematical construct used to estimate the physical quantity, ϕ. The Laplace equation for ϕ implies an algebraic difference equation for Φ. The spatial position of a mesh point is denoted by (i,j,k), with $x = i\Delta$, $y = j\Delta$ and $z = k\Delta$. The x derivative of ϕ to the right of the

---

[2] The function U_m should not be confused with the vector potential.

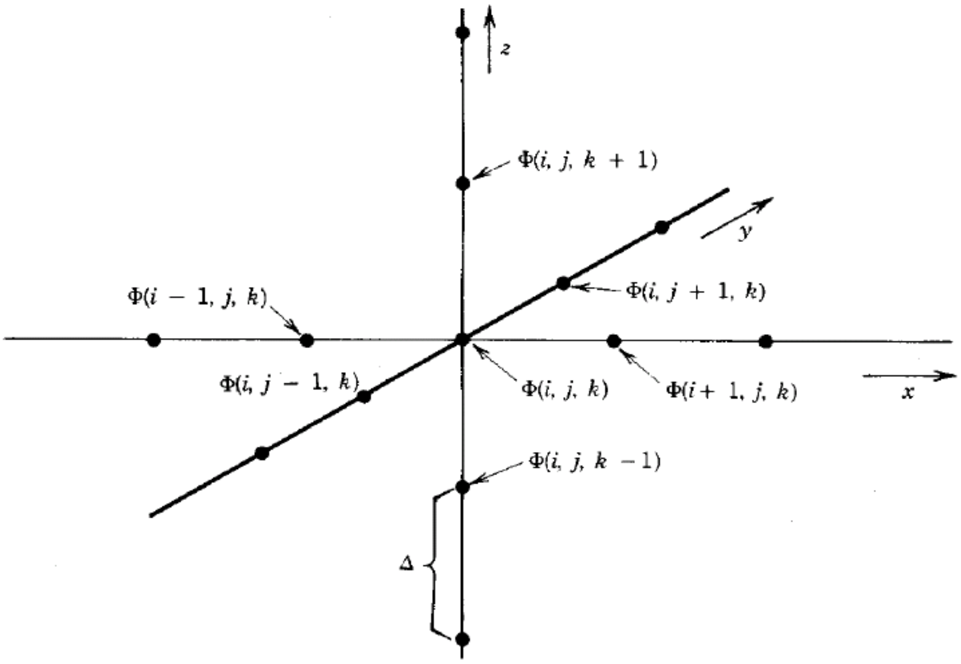

Figure 4.6: *Finite difference approximation for electrostatic potential.*

point (x, y, z) is approximated by

$$\partial\phi(x + \Delta/2)/\partial x = [\Phi(i + 1, j, k) - \Phi(i, j, k)]/\Delta$$

A similar expression holds for the derivative at $x - \Delta/2$. The second derivative is the difference of derivatives divided by Δ, or:

$$\frac{\partial}{\partial x}\left(\frac{\partial\phi(x)}{\partial x}\right) \simeq \frac{1}{\Delta}\left(\frac{\partial\phi(x + \Delta/2)}{\partial x} - \frac{\partial\phi(x - \Delta/2)}{\partial x}\right)$$

Combining expressions,

$$\frac{\partial^2\phi}{\partial x^2} = \frac{\Phi(i + 1, j, k) - 2\Phi(i, j, k) + \Phi(i - 1, j, k)}{\Delta^2}.$$

Similar expressions can be found for the $\partial^2\phi/\partial y^2$ and $\partial^2\phi/\partial z^2$ terms. Setting $\nabla^2\phi = 0$ implies

$$\Phi(i, j, k) = \frac{1}{6}[\Phi(i + 1, j, k) + \Phi(i - 1, j, k)+$$

$$\Phi(i,j+1,k)+\Phi(i,j-1,k)+ \tag{4.7}$$

$$\Phi(i,j,k+1)+\Phi(i,j,k-1)].$$

In summary, 1), $\Phi(i,j,k)$ is a discrete function defined as mesh points, 2), the interpolation of $\Phi(i,j,k)$ approximates $\phi(x,y,z)$ and, (3), if $\phi(x,y,z)$ satisfies the Laplace equation, then $\Phi(i,j,k)$ is determined by equation 4.7. According to equation 4.7, individual values of $\Phi(i,j,k)$ are the average of their six neighboring points. Solving the Laplace equation is an averaging process; the solution gives the smoothest flow of field lines. The net length of all field lines is minimized consistent with the boundary conditions. Therefore, the solution represents the state with minimum field energy.

There are many numerical methods to solve finite difference form for the Laplace equation. In this work, we have concentrated on the *method of successive over-relaxation* [21]. Although it is not the fastest method of solution, is has the closest relationship to the physical content of the Laplace equation. To illustrate the method, it is convenient to formulate the problem on a two-dimensional, square mesh (a graphical example is given in the Appendix). Successive over-relaxation is an iterative approach. A trial solution is corrected until it is close to a valid solution. Correction consists of swapping through all values of an intermediate solution to calculate *residuals*, defined by

$$R(i,j)=\frac{1}{4}\left[\Phi(i\pm 1,j)+\Phi(i,j\pm 1)\right]-\Phi(i,j), \tag{4.8}$$

where $\Phi(i\pm 1,j)$ stands for $\Phi(i+1,j)+\Phi(i-1,j)$, and similarly $\Phi(i,j\pm 1)$. If $R(i,j)$ is zero at all points, then $\Phi(i,j)$ is the desired solution. An intermediate result can be improved by adding a correction factor proportional to $R(i,j)$,

$$\Phi(i,j)_{n+1}=\Phi(i,j)_n+\omega\, R(i,j). \tag{4.9}$$

The value of ω can be set between 1 and 2, for obtaining a faster convergence. The algorithm stops when $R(i,j)$ is zero at all the mesh points.

4.4.2 Dipole Field

The fringe field of the PRISMA dipole magnet has been calculated using the Finite Elements Method fixed up with the field maps provided by the company Danfysik[3] which constructed the magnets. Danfysik mapped the fringing field at entrance and at exit of the magnet on the median plane and at two planes, located 5 cm above and below the median plane, with 2 cm steps for the mapping. The profile of the field and the field map, provided by the Danfysik are shown in Fig. 4.7. The profile of the fields have been parametrized with a Fermi-like function,

$$B_z = B_{max}\,\frac{1}{1+\exp(a\,x^3+b\,x^2+c\,x+d)},$$

whose parameters a, b, c, d have been calculated by means of a best fit over the map provided by the constructor.

Danfysik provided the maps for the main component of the magnetic field, B_z, therefore it has been necessary to calculate the components B_x and B_y in order to obtain a reliable simulation of the full magnetic field. On the basis of the Maxwell equations, by means of a Taylor expansion, we expressed B_x and B_y in terms of $B_z(0)$, which has been taken from the maps:

$$\begin{aligned} B_x(h) &= B_x(0) + h\,\partial_z B_x(0) + \frac{1}{2}h^2\,\partial^2_{z^2}B_x(0) + \frac{1}{6}h^3\,\partial^3_{z^3}B_x(0) + \mathrm{o}(h^4) \\ &= 0 + h\,\partial_x B_z(0) + 0 + \frac{1}{6}h^3\,\partial^2_{z^2}\partial_x B_z(0) + \mathrm{o}(h^5) \\ &= h\,\partial_x B_z(0) - \frac{1}{6}h^3\,\partial_x(\partial^2_{x^2} + \partial^2_{y^2})B_z(0) + \mathrm{o}(h^5) \end{aligned}$$

Analogously:

$$B_y = h\,\partial_y B_z(0) - \frac{1}{6}h^3\,\partial_y(\partial^2_{x^2} + \partial^2_{y^2})B_z(0) + \mathrm{o}(h^5)$$

These expressions have been implemented in our simulations, using the discrete differential operators described in the previous sections.

---

[3] Danfysik A/S, Jyllinge, Denmark

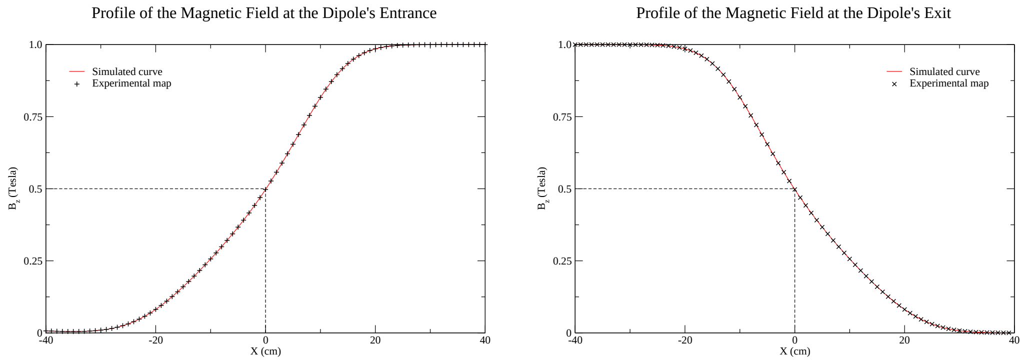
Profile of the Magnetic Field at the Dipole's Entrance

Profile of the Magnetic Field at the Dipole's Exit

Figure 4.7: *Measured dipole field profiles at the median plane of the entrance (left) and exit (right) windows, in the fringing regions. Here the B_z component of the field is shown, along an axis perpendicular to the window. The dotted lines, at $X = 0$, correspond respectively to the entrance and the exit windows.*

4.4.3 Quadrupole Field

The ideal quadrupole magnetic field is defined by the equation

$$\vec{B} = \vec{\nabla}\, U_m,$$

where

$$U_m = \frac{B_{max}}{R}\, x\, y$$

is the magnetic potential.

The PRISMA quadrupole fringing fields have been calculated by applying the over-relaxation method, that has been briefly described in the previous sections, on a rectangular three-dimensional lattice, big enough to contain the whole magnet (whose inner dimensions are 32 × 32 × 50 cm^3) and the mirror plate. This lattice was 100 × 100 × cm^2 large, at the base, and 150 cm depth, and was subdivided in a cubic mesh made of 1 × 1 × 1 cm^3 cells, to which were associated the values of the magnetic potential U_m.

The reliability if the relaxation method depends on how accurate is the model of the magnet "immersed" in the lattice. The shape of the poles, for instance imposes the boundary conditions that finally determinate the field lines. In this case the geometry of the poles (four hyperbolas, as depicted in Fig. 4.8, with faceted surfaces, see chapter 2) have been accurately reproduced, according to the specifications provided by the Danfysik company. In Fig. 4.8 is shown the model that has been used. The mirror plate placed in front of the entrance window of the magnet has been reproduced as well.

On the poles surfaces, a constant potential, calculated on the basis of equation 4.4.3, has been imposed, while in the mirror plate, as well as on the boundaries of the lattice, a zero potential has been fixed.

The relaxation method has been applied to the inner part of the magnet as well as in the fringing regions. A plot of the calculated field profile, compared with the measured field provided by the company, is shown in Fig. 4.9. A picture showing the reliability of the algorithms for the ion tracking is shown in Fig. 4.10.

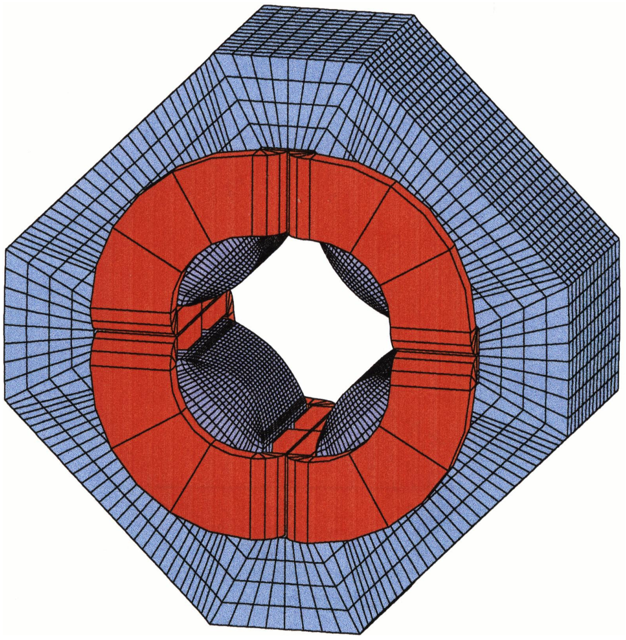

Figure 4.8: *The Finite Element model used for the simulation of the quadrupole fringing fields.*

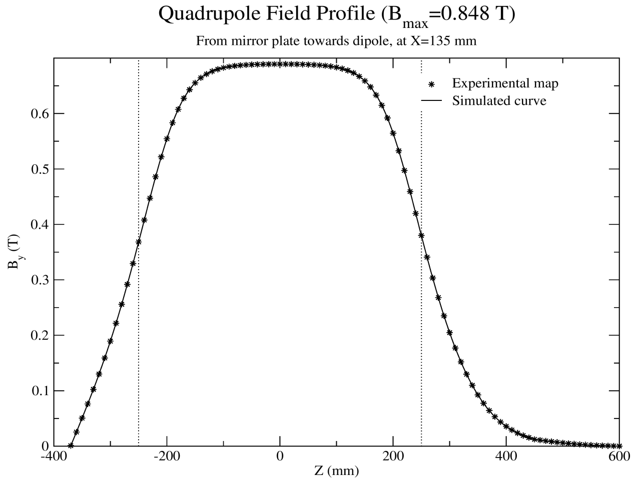

Figure 4.9: *Measured quadrupole field profile at 135 mm from the central axis. Here the* B_y *component of the field is shown. The dotted lines at* $Z = -250$ *mm and* $Z = 250$ *mm correspond to the entrance and the exit windows, respectively.* $Z = 0$ *corresponds to the center of the magnet. The continuous line indicates the simulated fields.*

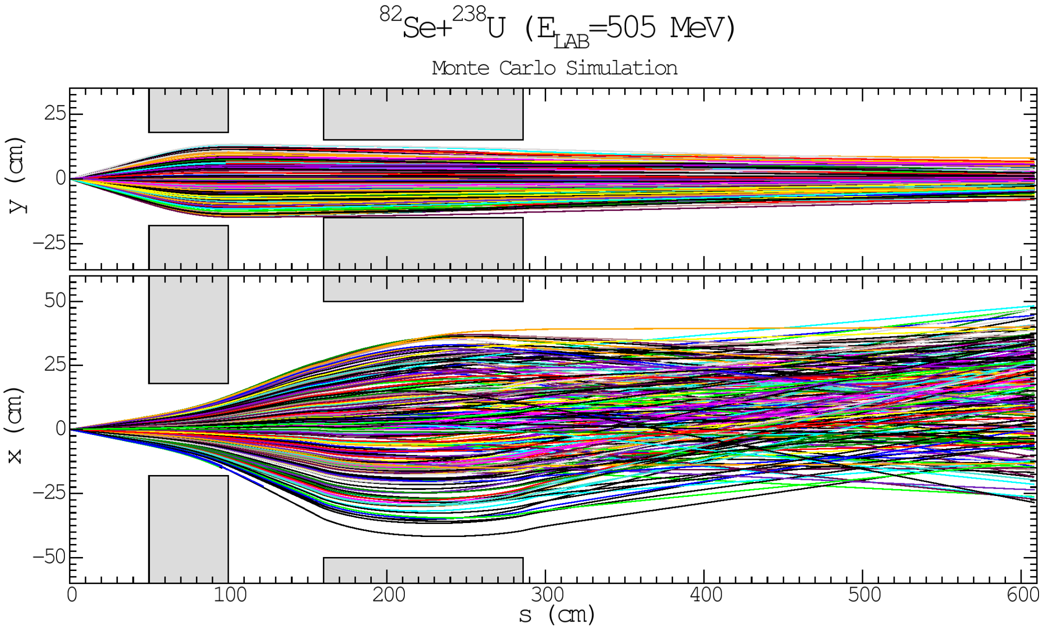

Figure 4.10: *Monte Carlo simulation of Rutherford events for the reaction* ^{82}Se *on* ^{238}U *at 505 MeV. The ion trajectories are represented in central trajectory coordinates (see the Appendix for details). The magnet poles are represented with gray boxes.*

Chapter 5

Data Analysis Techniques

5.1 On-line Monitoring

The on-line analysis is necessary for tuning the spectrometer for the particular need of the specific reaction and for detecting all possible problems that may influence the data taking, during the experiment, e.g., the beam current can decrease, the target could fail, or the detectors may not work properly. In order to save beam-time, all these conditions must be detected and handled promptly by the experimentalists. The way for checking the status of the spectrometer and of the data flow, is monitoring and taking under control the signals coming out from the detectors. As described in the previous chapter, all the signals are handled by the VME crate and sent to a farm of Linux computers, that takes care of collecting, histogramming and displaying the data; it is through this software that the user checks the reliability of the instrument at any time.

We now examine the most common problems encountered, during a run, by the different detectors. The focal plane position detector (PPAC) may show reduction of efficiency, especially with light ions, e.g., not all the ten independent sections have the same efficiency, or there can be inconsistencies within the acquired events, for example a missing TOF, for one or more sections. Inefficiencies within the position detectors can be detected by displaying the ten sections in a single histogram. The spectrum of Fig. 5.1, shows a clear inefficiency in the fifth section of the PPAC.

Fig. 5.2*(a)* shows an on-line two-dimensional plot X_{Left} vs. X_{Right} for a particular section of the PPAC. The 45^o band checks the reliability of the detector during the beam time. Fig. 5.2*(b)* shows an example of a scatter plot of the horizontal position X in the focal plane vs. the entrance angle θ. The bands correspond to different charge states of elastically scattered ions. The slight curvature in the charge state band is due to the optical aberrations, which anyway will be corrected by software.

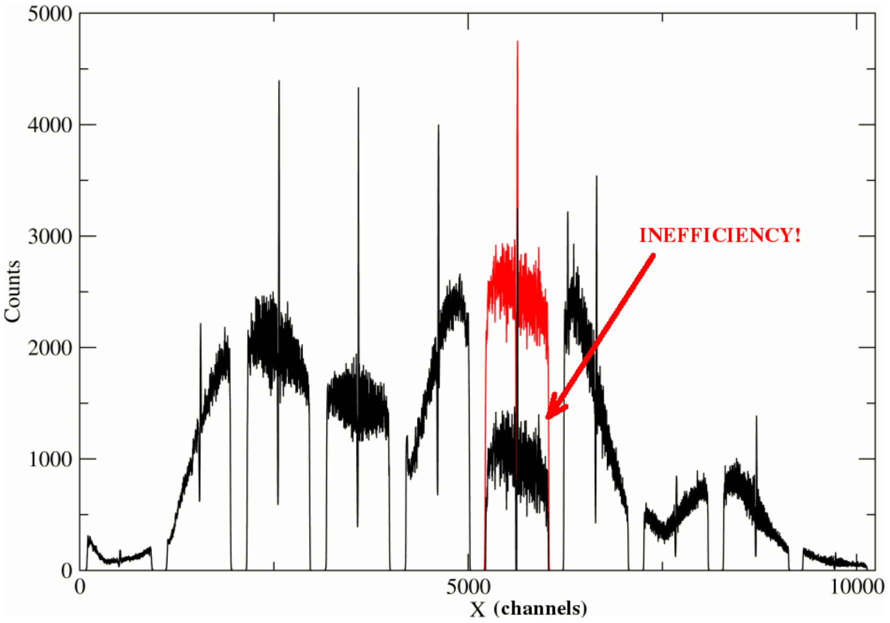

Figure 5.1: *Experimental position spectrum for the whole focal plane detector. An inefficiency in the fifth section is clearly visible. In red, how the spectrum should look like.*

The entrance position detector is near the target and risks to get overloaded by the incoming flux of reaction products, such as X-rays, γ, electrons and recoil ions. Nevertheless its efficiency has been measured to be nearly 100%, in typical reactions studied recently.

The ionization chambers need to be kept under control as well. The contamination of the filling gas may lead to a loss of resolution. Gas contaminants, such as oxygen, may capture the electrons formed by the ionizing particle thus reducing the signal amplitude at the anode. This is seen, in the on-line histograms, as a worsening in the resolution of the spectrum. This problem always appears and must be solved by re-filling periodically the chambers with new, “fresh”, gas. Due to the large volume of the the IC it was found sufficient to change gas once in 24 h. Dedicated systems for continuous gas flowing in the IC (and in the MWPPAC as well) will be implemented in PRISMA very soon.

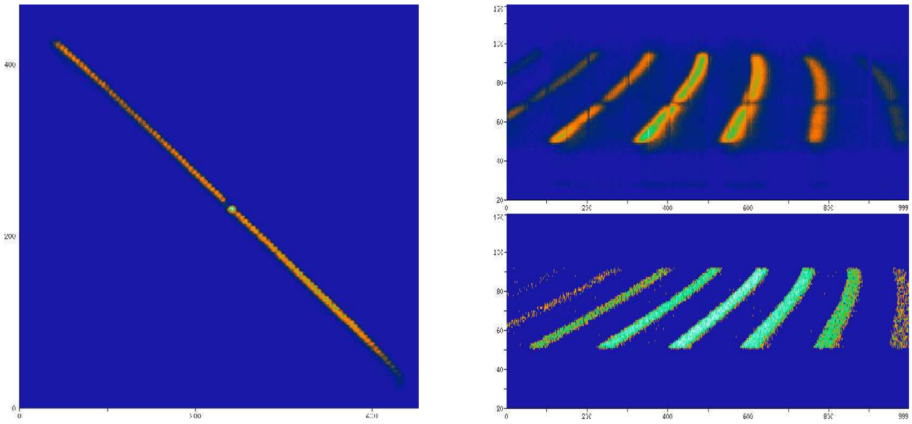

(a) *(b) up, (c) down.*

Figure 5.2: *(a) X_{Left}(PPAC) vs. X_{Right}(PPAC); (b) Two-dimensional scatter plot of position in the focal plane (PPAC) vs. entrance angle (θ), for the test run $^{56}Fe+^{197}Au$ at 186 MeV and $\theta_{\mathrm{PRISMA}} = 70^o$ (notice: the energy of the beam is below the Coulomb Barrier, therefore the projectiles are elastically scattered); (c) A computer simulated version of the same picture as (b).*

5.2 Off-line Data Analysis

As described in the previous chapter, the hundreds of signals coming from the detectors are handled by the VME crate and sent to a farm of Linux computers, through a PCI/VME interface. The acquisition software, running on the Linux farm, takes care of collecting, histogramming and displaying the data; this software allows to interact with the data for the on-line and off-line analysis. The purpose of PRISMA is the complete identification of the nuclides, i.e. their mass and atomic number. While the atomic number Z is obtained from the IC signals, the mass is not directly measured but must be reconstructed using the information from the MCP, PPAC and IC detectors.

For this reason it is necessary to “reconstruct” the physical information contained in every event, before proceeding with the actual off-line analysis. During the off-line data analysis, one needs this physical information for the final ray-tracing and mass reconstruction procedures; in fact, exact position (θ, ϕ) information from the entrance detector is necessary for tracing the trajectory. Moreover, for the determination of the absolute cross section or the relative yield of different reaction products, knowledge of charge state of the reaction products is necessary.

The package created for the off-line data analysis provides tools which take care of this event reconstruction. Tools have been created to process and convert the raw data files into binary data files, in which the physical parameters are directly stored in a proper data structure. Every detector must be treated separately and in a different way, depending on its working conditions and on the kind of signals it is providing.

5.2.1 prismaCalibration

Several measurements are required to identify the products of a reaction: the ion entrance position, the position after the magnets, the time of flight and the energy and the energy loss from the ionization chambers. During the on-line acquisition, the data are stored, on tape and/or on disk, in a *raw* format (i.e. as they come from the buffers of the data acquisition system). Thus, before starting the physical data analysis, the raw data must be calibrated, made linear and merged in order to obtain the physical information event by event. To perform these operations, as quickly and easily as possible, a graphical program has been created (see Fig. 5.3). This program is just

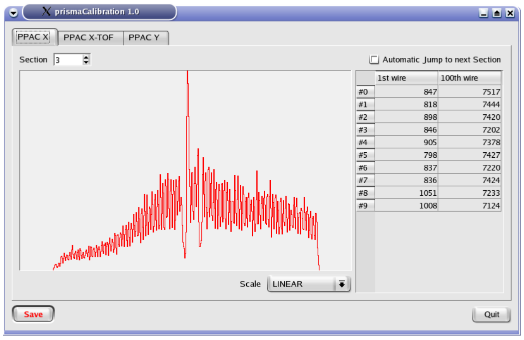

Section 3

	1st wire	100th wire
#0	847	7517
#1	818	7444
#2	898	7420
#3	846	7202
#4	905	7378
#5	798	7427
#6	837	7220
#7	836	7424
#8	1051	7233
#9	1008	7124

Scale LINEAR

Figure 5.3: *"prismaCalibration" easily calibrates the raw signals. Here the user can calibrate the position focal plane detectors.*

a graphical interface relying on many different sub-tools that take care of properly managing the signals of the detectors.

Entrance detector. A mask has been placed parallel to the carbon foil (CF) and about 1 cm downstream of the CF in order to perform a geometrical calibration (see Fig. 5.4). From this two dimensional matrix a table has been extracted with the correspondences between the pair of coordinates in units of channels and their coordinates in millimeters with respect to a known reference system (i.e., the laboratory frame). In principle, this "in beam" calibration of the entrance detector should be repeated for every experiment, but it has been found that the resulting X vs. Y matrix does not really change from one run to the next. For this reason, it is enough to check such a calibration procedure only once in a while.

Focal plane position detector. The PRISMA focal plane position detector is made by ten independent sections, each one 10 cm large (the total focal plane is 1 meter long). In each section, the position information is obtained from the time difference between the signals from the left and right of the delay lines (namely X_{Left} and X_{Right}) of each section (see Chapter 2). This

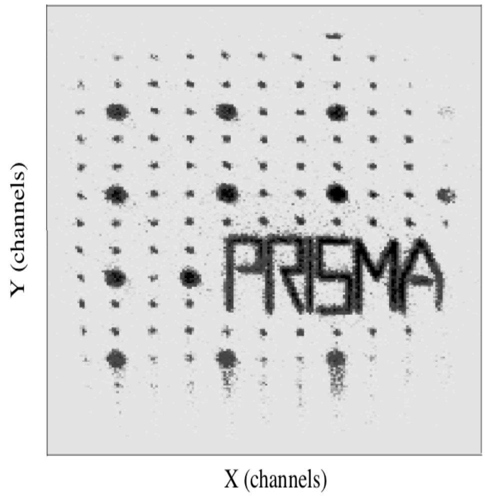

Figure 5.4: *The image of the mask obtained during the in-beam test. The mask was placed on the carbon foil of the detector. The counts are shown in a log scale. In this case we have two diameters for the mask holes, i.e. 3 mm and 1 mm. The holes are 5 mm apart from each other.*

means that, for each section (i), the position $X_{(i)}$ is calculated as:

$$X_{(i)} = X_{(i)\text{Right}} - X_{(i)\text{Left}}.$$

This quantity is within the range $[-4095, 4095]$, but normally occupies a smaller range. For numerical reasons, it is convenient to move it into the interval $[0, 8191]$. A typical spectrum is shown in Fig. 5.5. Then, the position information for each section, provided by the acquisition system must be converted from units of channels into a distance, in units of length, with respect to a convenient frame of reference. This operation consists in "stretching" the spectra and "gluing" them together. The program "prismaCalibration" accomplishes this task is a very user-friendly way, i.e. by means of a graphical window where the user can perform these operations by using the mouse.

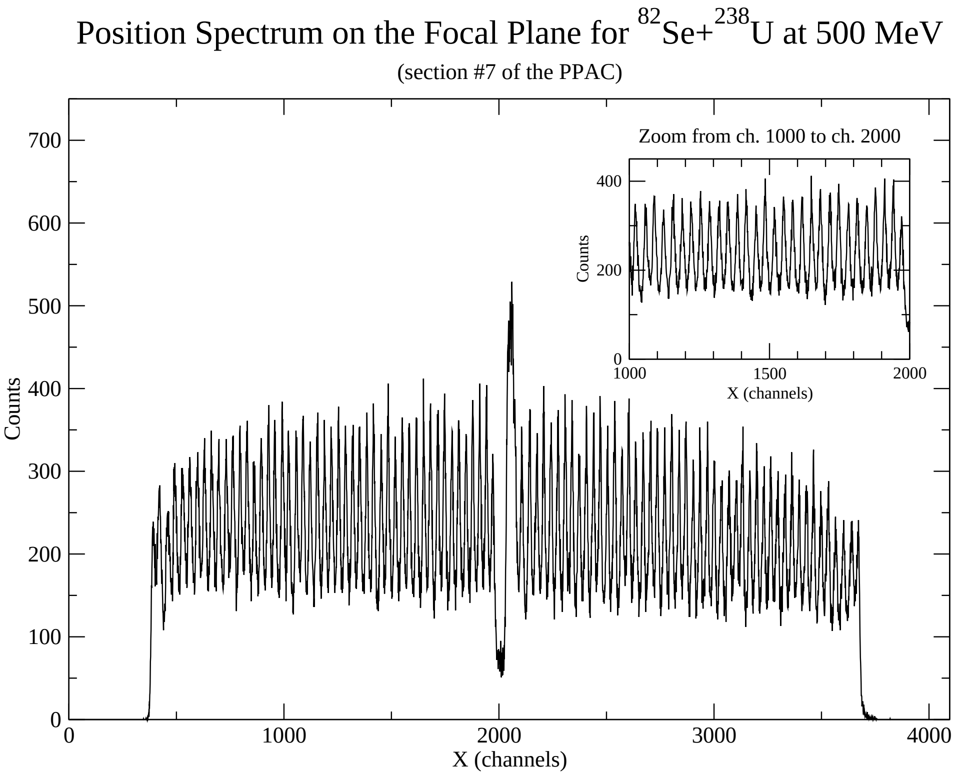

Figure 5.5: *X position spectrum measured in one of the ten sections of the MW-PPAC, for* ^{82}Se+^{238}U *at 505 MeV. In the top-right window, a detail showing the individual wires. The two central wires have been joined together for reference, thus causing the central peak and dip.*

5.2.2 prismaAnalysis

The analysis of a data file is a complex process, made in several steps that must be executed in a precise order (see Fig. 5.6). The “prismaAnalysis” program takes care of collecting all the necessary information before performing the trajectory reconstruction. This program leads the user through the analysis process asking for his cooperation only when automatic decisions cannot be taken.

In the following figures, the main steps are shown. Fig. 5.7 shows the first panel proposed to the user by the program. In this window the user must

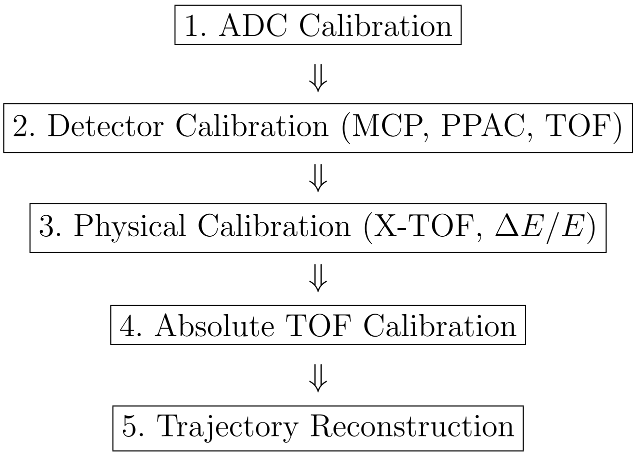

Figure 5.6: *The analysis process consists of five steps.*

provide the main parameters of the reaction, such as the angle of PRISMA, the magnetic field intensity, the energy of the beam, the thickness of the target and the identity of the reacting particles. This information teaches the program about the key quantities important for the reaction, and will be used in the next steps of the analysis.

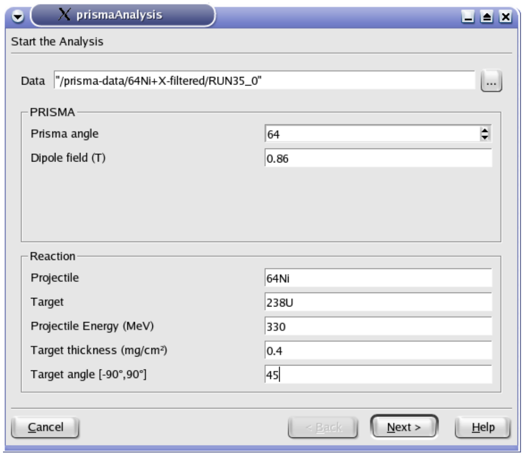

Start the Analysis

Data "/prisma-data/64Ni+X-filtered/RUN35_0"

PRISMA

Prisma angle: 64
Dipole field (T): 0.86

Reaction

Projectile: 64Ni
Target: 238U
Projectile Energy (MeV): 330
Target thickness (mg/cm²): 0.4
Target angle [-90°,90°]: 45

Figure 5.7: *Setting up the reaction parameters.*

After this step, the program asks the user to partition the entrance solid angle by setting slices in the entrance θ angle. Using this information, the program creates a stack of X-TOF matrices, one for each slice defined by the user. Any X-TOF matrix, as it is known, represents a mass/charge (A/q) spectrum. For each matrix, the user is now required to highlight the main A/q lines, in order to set the parameters for linearizing them(see Fig. 5.8). The program is now able to compute the A/q ratio for any entrance angle, focal plane position and time of flight, event by event, interpolating between the different slices. It must be noticed, that the tagging of the X-TOF matrix

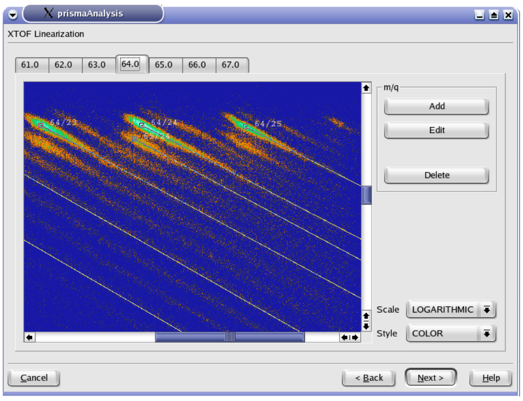

Scale LOGARITHMIC
Style COLOR

Figure 5.8: *X-TOF matrix for a particular selection in the entrance angle.*

is not necessary for the success of the trajectory reconstruction algorithms, because the code identifies the events, no matter which point it is starting from in the configuration space, but it is worth to make it because it will speed up the convergence.

The definition of the Z-lines is the next step. A window showing the ten $\Delta E/E$ matrices for all sections of the ionization chamber is presented. The user is now required to identify at least two Z-lines (one of them could correspond to beam particles) for each one of them. The identification is made by defining a polygonal line with the mouse (see Fig. 5.9). For each section it is also possible to exclude the regions where the Z-lines are overlapping, or where the Z identification could be difficult or ambiguous. According to the indications of the user, the program linearizes the Z-lines, and creates a Z coordinate. In Fig. 5.10(left) the resulting A/q vs. Z matrix is shown, for one of the recent experiments. The ambiguity in the ion charge state q will be solved by using the independent information coming from the energy E of the ionization chambers. As a matter of fact, in a representation E vs. x (the position along the focal plane), for each selected Z, the various charge states are clearly separated at least for the most intense channels, as shown in the example of Fig. 5.10(right). Once q has been identified, distributions of Z, A and reconstructed energy can be produced, and subsequently summed over q, if needed.

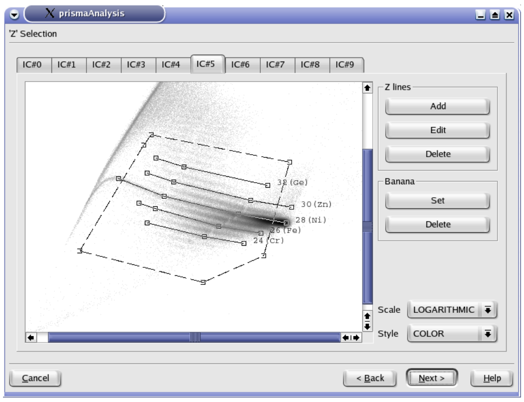

Scale LOGARITHMIC

Style COLOR

Figure 5.9: *Defining the Z-lines.*

Absolute TOF Calibration

The time of flight signal measures the time interval between the start and the stop signals coming from the entrance and the focal plane detectors (see chapter 2). “prismaCalibration” allows the alignment of different TOF signals coming from the ten PPAC sections but, in order to perform the full ion tracking, it is necessary to find out the *absolute offset* for the time of flight.

For a given event ’e’, the absolute offset is calculated, $\Delta TOF_{[\mathrm{e}]}$, as the difference between the real (i.e. calculated) $TOF_{[\mathrm{e}]}$ and the measured $\mathrm{TOF}_{[\mathrm{e}]}$:

$$\Delta TOF_{[\mathrm{e}]} = TOF_{[\mathrm{e}]} - \mathrm{TOF}_{[\mathrm{e}]}.$$

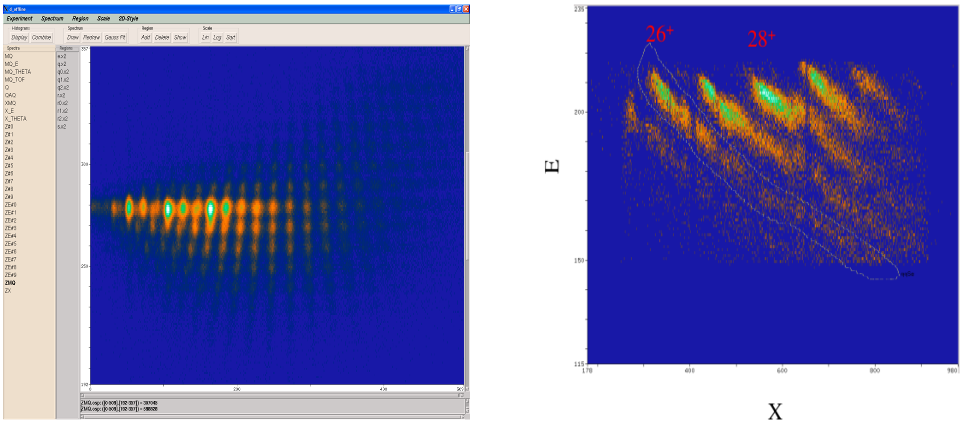

Figure 5.10: *Two-dimensional spectra* A/q *vs.* Z *for* ^{64}Ni + ^{238}U *(left), and* X *vs. energy for* ^{82}Se + ^{238}U *(right).*

The problem is to deduce the actual time of flight from the measured signals. From the equation

$$B\rho = \frac{p}{q},$$

where

$$\frac{p}{q} = \frac{m\,v}{q} = \frac{m}{q}\frac{S}{TOF}$$

one obtains

$$TOF = S\frac{m}{q}\frac{1}{B\rho}.$$

Thus, if the length of the trajectory, the $B\rho$, and the m/q are known, then it is possible to calculate the absolute TOF. Following what has been described in the previous chapter, it is clear that both the path length S and the radius of curvature ρ can be determined by means of the geometrical reconstruction of the trajectories. In fact, this algorithm gives a reliable approximation both for S and ρ, when applied to the central trajectories. On the other hand, the X-TOF matrix provides the m/q ratio. Therefore, the absolute TOF can be calculated from the central trajectories. That is useful in order to calculate absolute mass values, with no need to calibrate the mass spectrum. An example of this system will be presented in the following chapter.

Resolving the Nuclear Charge State

As discussed chapter 3, paragraph 3.2.3 the nuclear charge state Z can be determined in the usual way, linearizing of the $\Delta E/E$ matrix. It must be noticed that the resolution depends only on the intrinsic resolution of the IC, while it is not affected by the energy loss and straggling in the entrance window. An important consideration here is the relative calibration of the different sectors of the IC, since a single trajectory may affect quite a few of them. To begin with, the gas pressure is adjusted in such a way that the ions fully stopped in the fourth row of section, and secondarily the trajectory may be such that it crosses to nearby side sectors (see Fig. 3.3 and 4.1). A careful calibration of the amplifiers and ADC's makes it possible to preserve a sufficient resolution even after summation of the different sectors (see Fig. 3.6).

Resolving the Ionic Charge State

For the q charge state identification, three basic relations between the measured quantities, energy loss ΔE, total energy E, flight time T and position of the focal plane X, are used:

$$\begin{aligned} T &= \frac{S(\theta,\phi)}{v}, \qquad B\rho = A \cdot \frac{v}{q} \propto X \\ E &= \frac{1}{2} A \cdot v^2 \end{aligned} \tag{5.1}$$

From these follows:

$$q = \frac{2}{S(\theta,\phi)} \cdot \frac{E \cdot T}{B\rho(\theta,\phi)}. \tag{5.2}$$

In spite of the fact that several signals have to be combined, the resolution is mainly determined by the total energy resolution of the focal plane detectors, which is deteriorated by the energy loss and straggling in the mylar windows. The optical aberrations are accounted for in the flight length $S(\theta,\phi)$, which, as it has been shown in the previous chapters, must be reconstructed event by event.

If we were in an ideal world, equation 5.2 would give directly the charge state q; unfortunately, this is not true. The two dimensional scatter plot of charge state q vs. A/q helps in understanding the problem and at the same time provides a mean to identify the charge state (see Fig. 5.11 for an old example taken from [37] with the GSI spectrometer, the same matrix, obtained with PRISMA, will be shown in the next chapter). In this picture, the horizontal structures correspond to individual masses with the same charge state (and the charge state shows a mass dependence). The distortions visible in the figure, may be due to the energy resolution of the chambers, which is moreover deteriorated by the energy loss of the ions in the entrance and exit windows of the PPAC, and in the entrance window of the IC. The fraction of energy released in the three windows, composed by a layer of Mylar 200 μg/cm^2 thick each one, depends on Z, M, and E of the incoming ions, and amounts to $\approx 20 - 30$ MeV.

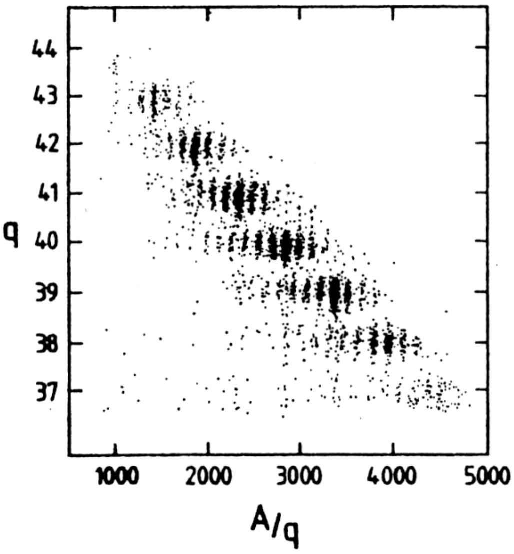

Figure 5.11: *Typical two dimensional scatter plot of charge state q vs. A/q. The vertical lines correspond to individual masses, whereas the horizontal lines correspond to different charge states q (for details about this figure see [37]).*

Sometimes the charge state cannot be determined unambiguously for any event: there exists the possibility of a misidentification of the charge state and this unfortunately produces spurious mass peaks which contribute to the "background" in the mass spectra. The problem depends entirely on the energy resolution of the IC and is most critical for heavy masses and low energies.

Trajectory Reconstruction

Once the program "prismaAnalysis" has collected almost all the necessary information, the ion tracking begins. The program just asks the user the file name in which the reconstructed events must be saved, then it starts. It must be noticed that the reconstructed parameters M, Z, q and E, will be stored together with their corresponding raw buffer, so that it is possible to re-sort the data for further analysis. For instance, while PRISMA is coupled with CLARA, studies of γ-spectroscopy on specific isotopes identified by PRISMA are possible making use of the software developed for Euroball and GASP throughout the last years (i.e. `gsort`, `xtrackn`, … [16]).

Chapter 6

Study of the Reaction 505 MeV ^{82}Se on ^{238}U

In the first half of the 2004, the first experiments with the spectrometer PRISMA have been performed. In this chapter the analysis of the reaction ^{82}Se+^{238}U at 505 MeV (close to the Coulomb barrier) is considered. The study of this system was proposed in order to investigate the production of neutron-rich nuclei in the vicinity of the expected double shell closure of ^{78}Ni, via multinucleon transfer collisions. We take this experiment as an example of the application of the data analysis techniques which are the main part of the present work. The result will show that a very accurate and efficient ion identification (in mass, Z and energy) has been accomplished using the off-line software for the treatment of the raw data.

6.1 The ^{78}Ni Region and the Stability of the Shell Gaps in Nucleon-rich Nuclei

In the whole nuclear chart only a few cases of magic nuclei are accessible to experimental studies. The structure of the nuclei in the neighborhood of double shell closures provides vital information of the effective interaction, through the single particle energies and the two-body residual interactions.

This information can be extracted from the nuclear structure of one and two valence nucleons systems. Core excitations across the shell gaps are also fundamental for our understanding of nuclear structure. It is of particular interest to study of how the structure evolves in a series of nuclei with a magic number of protons or neutrons, which lie between two shell closures of the other kind of nucleon (e.g. ^{56}Ni-^{68}Ni-^{78}Ni). The fact that only one of the two kinds of nucleon contributes to the low energy states, implies that the only isovector ($T = 1$) interaction plays a role in such states and this interaction can not generate quadrupole deformation. This property is well described in the framework of the generalized seniority scheme [43]. One example of the validity of this scheme is provided by the even-even Sn ($Z = 50$) isotopes, where the 0^+-2^+ spacing is constant from $N = 52$ to $N = 80$. The same effect should be found in the Ni ($Z = 28$) isotopes between the magic numbers $N = 40$ and $N = 50$. The population of nuclei in the vicinity of the ^{78}Ni is in principle possible in multinucleon (multi-proton) transfer reactions, as shown schematically in Fig. 6.1. Via multi-proton stripping channels one can in fact populate neutron-rich nuclei in the Ni region, and in principle get close to the nucleus ^{78}Ni, which is of great interest for future γ-spectroscopic studies. The difficulty in populating these extreme isotopes via multinucleon transfer in not only the low primary cross sections but the fact that as more nucleons are transferred the excitation energies of the fragments increase significantly and neutron evaporation effects modify the final yields in a significant way. The effects of nucleon evaporation from the primary fragments has been shown to play an important role in multinucleon transfer reactions (see [10] and references therein).

Several nuclear structure calculations [19, 25] predict radical changes in the shell structure of very neutron-rich nuclei. As we move away from stability, the shell gaps known in stable and proton-rich nuclei will gradually narrow and then disappear. The main reason for this change is the reduction of the spin-orbit interaction strength in nuclei with high diffuseness due to the large neutron excess.

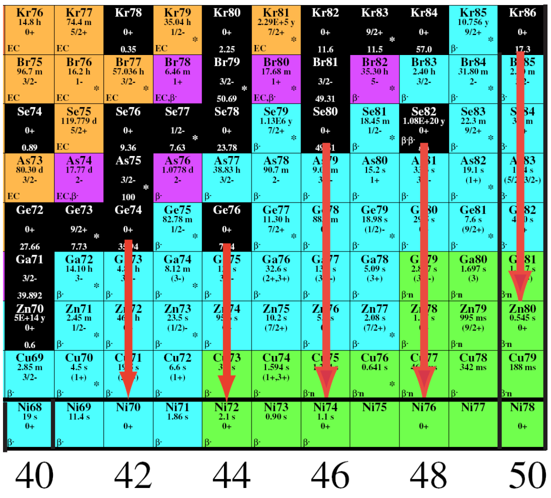

Figure 6.1: *The population of nuclei in the vicinity of doubly-magic ^{78}Ni in multinucleon transfer reactions.*

In particular it is predicted [32] that the starting point for this transition lies not very far from stability, in neutron-rich nuclei reachable by multinucleon transfer reactions. As an example, the calculations of R. Nayac [32] predict a reduction in the shell gap at $N = 50$, between ^{82}Ge and ^{80}Zn. A theoretical calculation performed with the code GRAZING [45] predicts for ^{82}Ge (-2p+2n channel starting from ^{82}Se) a cross section $\sigma > 200\mu$barn in multinucleon transfer reactions.

6.2 A Previous Test Run

Within this physical frame, a few years ago a test of ^{82}Se+^{238}U at an energy of 500 MeV was performed by using the Time-of-Flight spectrometer PISOLO [11]. A ^{82}Se average beam current of $\simeq$ 1 pnA was delivered on a ^{238}U target with a thickness of $\simeq 200\mu$g/cm^2. The yields of the main transfer channels, populated at different angles around the grazing angle, were measured.

Even with the limited PISOLO angular acceptance, transfer channels up to 8 proton stripping were observed at the grazing angle, in about 8 hours of beam time (see the experimental $\Delta E - E$ matrix depicted in Fig. 6.2). The mass resolution of PISOLO was not sufficient to distinguish the individual masses of transfer products, unfortunately.

From previous tests and taking into account the large acceptance of PRISMA (80 msr), and also requiring mass spectra with good or reasonable statistics for the many-proton stripping channels, four days of beam time were estimated necessary for an experiment with the new spectrometer, with a beam current of $\simeq 1$ pnA.

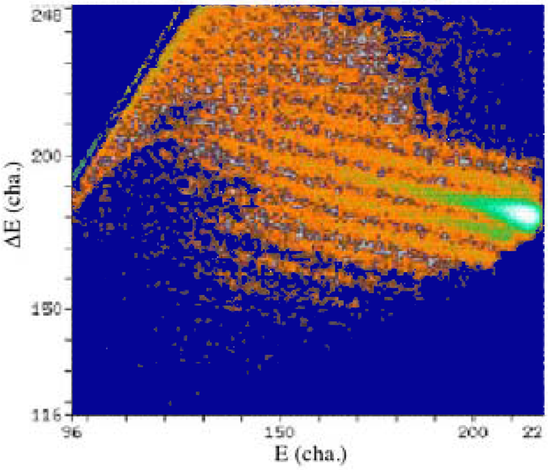

Figure 6.2: *$\Delta E - E$ matrix of ^{82}Se+^{238}U obtained at 90^o with PISOLO.*

Experimental Conditions

The PRISMA spectrometer was rotated to 64^o, which is an angle close the grazing angle for this reaction (that is $\simeq 67^o$ in the Laboratory frame). The target was a 1.55 mm strip of ^{238}U 400 μg/cm^2 thick, evaporated on a carbon-backing with a thickness of 28 μg/cm^2.

The quadrupole and dipole magnetic fields were set so that the most probable charge state of the beam-like ions (i.e. selenium) was bent and focused on the center of the focal plane. The most probable charge state $< q >$ for a beam of ions with atomic number Z, energy E, expressed in

MeV, and atomic mass A, can be estimated by [46]:

$$< q >= Z(1 + [Z^{-0.45} \cdot 3.85 \cdot \sqrt{E/A}]^{-1.67})^{-0.6}.$$

For a ^{82}Se beam at 505 MeV scattered to $\theta_{lab} = 64^o$ by a ^{238}U target, $< q >$ is 27+.

Further details about the experimental conditions and the beam's characteristics are summarized in Tab. 6.1.

REACTION & BEAM	
Projectile	^{82}Se at 505 MeV
Beam Current	1 pnA
Beam Spot Radius	≈ 2 mm
Target	^{238}U
Target Angle	45^o
Target Thickness	400 μg/cm^2 with C-backing (≈28 μg/cm^2)
Energy Loss in the Target	≈ 6.5 MeV
$< E >$ for ^{82}Se	320 MeV (calculated)

PRISMA	
Detection Angle	$\theta_{\mathrm{PRISMA}} = 64^o$
Dipole Field	63.99% max current intensity (≈0.705213 T)
Quadrupole Field	50.82% max current intensity (≈0.430945 T)
PPAC Filling Gas	Isobuthane (C_4H_{10})
PPAC Filling Pressure	7 mbar
IC Filling Gas	Methane (CH_4)
IC Filling Pressure	72 mbar

Table 6.1: *Summary of the experimental conditions.*

6.3 Analysis Procedure

The experiment lasted four days of beam time, and 330 GB of raw data were written by the data storage system. Here the analysis process is presented, from the sorting of the raw data to the mass spectra, and the final tagging of events with their proper Z, A, E and q quantities.

6.3.1 Filtering the Data

Raw data need to be filtered in order to remove the events where particles recoiling from the target have reached the focal plane. The cross section for the recoil ions is much larger than the cross section for ^{82}Se-like particles. Therefore these heavy ions trigger the data acquisition system much more rapidly than the light ones. The relative amount is approximatively 90% of recoils and %10 of interesting reaction products. Fortunately, it is quite straightforward to separate the "bad" recoil events from the "good" ones because recoils are usually slower. For this reason, their time of flight does not fit within the temporal window of the Time-to-Amplitude converters and then their structure on disk will result incomplete. Summarizing, "filtering" the data means removing all the events lacking the TOF information. This avoids the analysis of unwanted events and makes faster the analysis sessions.

6.3.2 Detectors Calibration

The signals coming from the PRISMA detectors have been calibrated and linearized in order to proceed with the off-line analysis procedures. In other words, the raw signals have been converted into a "physical event", i.e. a set $(x, y, X, Y, TOF, \Delta E, E)$, whose entries are expressed in their proper units, as far as this is possible.

Entrance Detector

The MCP output has been linearized and calibrated in order to provide a physical position information, in units of length, which is necessary to calculate the exact direction of the ions entering the spectrometer. To this end, a mask was placed in front of the MCP detecting area (see Fig. 6.3). A typical experimental X,Y matrix of the entrance detector is shown in Fig. 3.4 at page 35. The mask was a cross with four arms and four small flags, at a fixed distance from the center (4 cm), on each of the four arms. Thanks to this particular shape, it was possible to calibrate the MCP X,Y matrix, namely finding the center and the scale factor. This calculation was done by using two polynomials of the third degree, one for the X coordinate and one for the Y coordinate, calculated in order to fit with five reference points: the center and the four small flags.

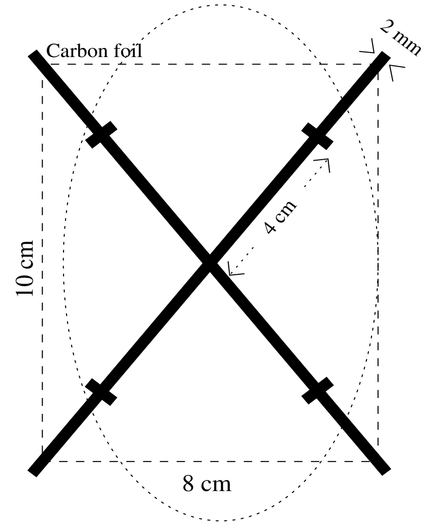

Figure 6.3: *The calibration mask placed in front of the detector (see text). The ellipse sketches the intersection between the cone corresponding to the acceptance of PRISMA and the detecting area of the MCP. The ellipse is not centered because was slightly off-axis in this experiment.*

Finally, it must be noticed that, since the crossing strips are only 2 mm wide, this mask does not significantly reduce the entrance solid angle of the spectrometer and for this reason was kept during all the experiments.

Focal Plane Detectors

The calibration of focal plane detectors proceeded as described in the previous chapters. The computer program **prismaSort**, can easily set the necessary parameters for stretching and translating opportunely the ten position spectra. Then the ten time of flight signals were aligned with respect to the each other. Fig. 6.4 shows how the X-TOF matrix did look like before (left) and after the time of flight calibrations (right).

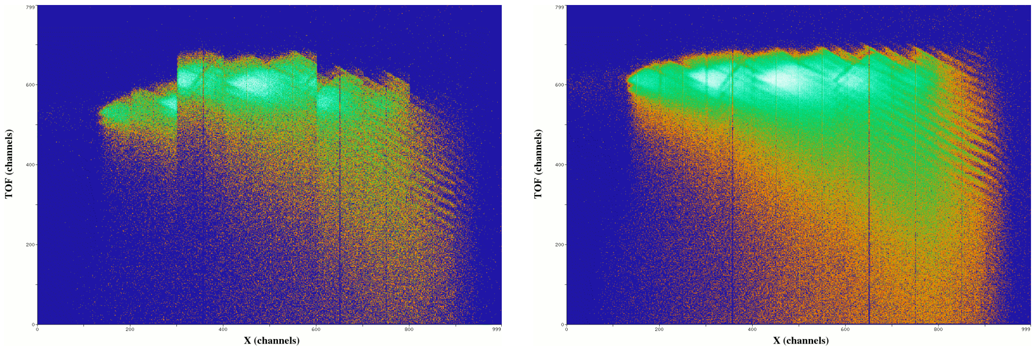

Figure 6.4: *Time of flight vs.focal plane X position for this reaction. The left panel shows the matrix before the alignment of the ten time of flight signals, whereas the right panel shows the same matrix after the calibration.*

The prismaAnalysis program calculates also the absolute TOF offset calibration, by means of the geometrical approximation for the central trajectories described in Chapter 4. The resulting offset was calculated by averaging the result of 10000 trajectories. The result is:

$$\Delta TOF = (235.33 \pm 1.61)\ \text{ns}.$$

6.3.3 Resolving the Nuclear Charge State

The nuclear charge Z could be determined in the usual way, that is by means the energy loss/energy ($\Delta E/E$) matrix of the ionization chambers. The resolution of the ionization chambers is in principle sufficient to guarantee a resolution $\Delta Z/Z$ of $\approx 1/50$, which is enough for the experiment under study. Therefore, the $\Delta E/E$ scatter plot were mapped by labeling some Z lines.

Actually several reasons may have influenced the energy resolution in this experiment: the 400 μg/cm^2 thick target and its inhomogeneities, for instance, introduced a non-negligible kinetic energy loss and straggling, about 6.5 MeV (i.e. $\approx 2\%$ of the total kinetic energy). Furthermore, $\simeq 30-35$ MeV were lost in the three Mylar windows (in total 600μg/cm^2) in front of the IC. All this led to a Z resolution in the $\Delta E/E$ scatter plots, which was not optimal.

Besides that, another difficulty raised in the identification of the $Z = 33$ (arsenic) events. Being the Z line of this nucleus just below the one corresponding to the elastic plus inelastic channel ^{82}Se ($Z = 34$), the identification of $Z = 33$ was not unique over all the energy range. This problem was partially solved putting suitable "veto" gates on the problematic areas of the $\Delta E/E$ matrix.

6.3.4 Resolving the Ion Charge State

The q charge state identification has been calculated with the algorithms described in the previous chapters. Although the procedure is fully automatic, being based on the tracking algorithms, in this case was necessary to put additional gates on the scatter plot A/q vs. q, in order to avoid the non-linearities that could have badly influenced the mass identification particularly for the weak channels. The A/q vs. q scatter plot is shown in Fig. 6.5). Referring to the cited [46], we know that the most probable charge state of the charge distribution is $< q >= 27^+$; then, it is straightforward to assign the correct charge state to each bunch of events visible in the q vs. A/q

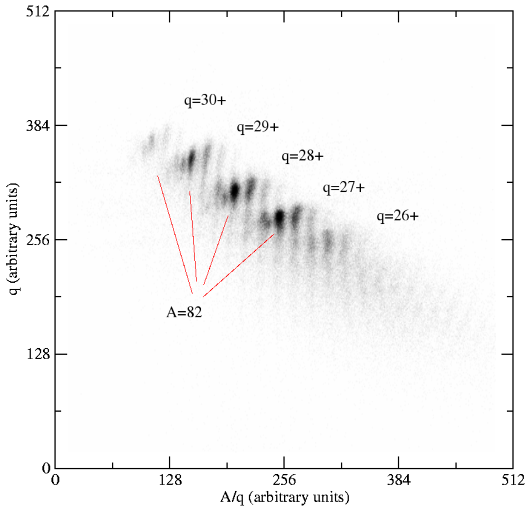

Figure 6.5: *Two dimensional scatter plot of charge state* q *vs.* A/q *for this reaction. The vertical lines correspond to individual masses, whereas the horizontal lines correspond to different charge states* q.

matrix. The charge states were labeled by means of gates. The reconstruction algorithms provide a method for checking the correct assignment of the charge states. They provide the reconstructed mass M in atomic mass units, therefore any error in the charge state assignment would produce a shift in the mass spectra, that would be noticed in the mass of the elastic peak.

For this reaction, eight charge states have been assigned, that is q from 23^+ to 30^+. In the scatter plot of Fig. 6.5, the most populated charge states, 25^+ to 30^+, are the most visible ones, but even the lower charge states, such as 23^+ or 24^+, can reasonably be identified, in a logarithmic scale.

6.4 Evidence of Nucleon Transfers

Following ion trajectory reconstruction, the final mass spectra are shown in Fig. 6.10 and the region of the Chart of Nuclides that has been populated by the reaction is visually reported in Tab. 6.6. The reported "counts" are the number of events associated with a particular (Z, A) combination (see also Appendix A.3), where the identification (through ion tracking) was performed for the $\simeq$ 10% of the total statistics accumulated in the experiment. There is no normalization to an absolute cross section scale. This further analysis goes beyond the aim of the present work.

These results show the reliability of the algorithms discussed in the previous chapters. The mass resolution in this experiment was

$$\frac{\Delta A}{A} \cong \frac{1}{250} \quad \text{(FWHM)}. \tag{6.1}$$

In Fig. 6.10 the mass distribution for selenium isotopes is shown in red.

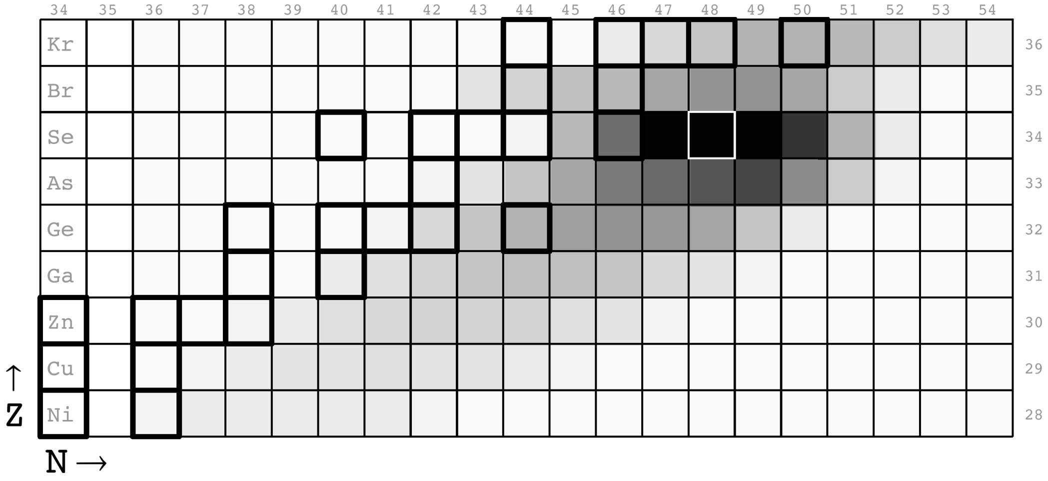

Figure 6.6: *Region of the Chart of Nuclides populated by the reaction* ^{82}Se+^{238}U. *The stable nuclei are highlighted by black contours. The projectile is highlighted in white.*

Fig. 6.7 shows the angular distribution for the most important transfer channels observed in the same reaction in the previous test experiment with the spectrometer PISOLO, where the resolution in Z was good enough. PRISMA, has a high resolution in mass, and its 12^o wide angular acceptance in θ_{lab} (see the red lines in Fig. 6.7), cover most of the quasi-elastic transfer flux when the spectrometer is set at $\theta_{lab} = 64^o$, as in this experiment.

A further interesting aspect of the reaction is obtaining the Q-value dis-

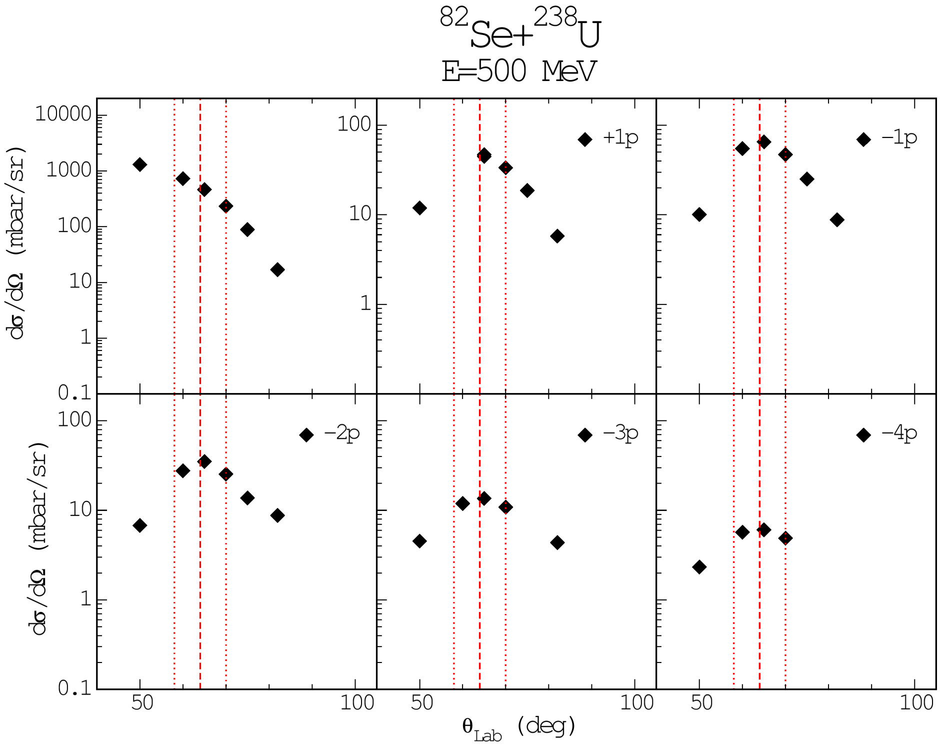

Figure 6.7: *Angular distribution for the most important channels of the reaction* ^{82}*Se*+^{238}*U, for the previous experiment with PISOLO. On the top-left frame the elastic+inelastic differential cross sections are plotted. The dashed red line indicates the central angle* $\theta = 64^o$ *to which PRISMA was set for the current experiment. The dotted red lines subtend an angle as wide as the* θ *acceptance of PRISMA (please notice the logarithmic scale).*

tributions. The Q-value, for a binary reaction, can be obtained from

$$Q = \frac{M_3 + M_4}{M_4} E_3 - \frac{M_4 - M_1}{M_4} E_1 - \frac{2\sqrt{M_1 M_3 E_1 E_3}}{M_4} \cos\psi \tag{6.2}$$

where:

M_1/E_1	mass/energy of the incident particle
M_3/E_3	mass/energy of the light reaction product
M_4	mass/energy of the heavy reaction product
ψ	the scattering angle in the laboratory frame.

Starting from this, the total kinetic energy loss (TKEL) for the reaction, defined as the difference between the ingoing and the outgoing kinetic energies, is simply

$$TKEL = -Q. \tag{6.3}$$

TKEL distributions for some representative transfer channels are shown in Fig. 6.8. Such TKEL are derived assuming a pure binary process and no correction has been applied for nucleon evaporation from the fragments. From the figure, one sees that the distribution for the one-neutron pick-up channel has its major contribution close to the optimum Q-value ($Q \simeq 0$ MeV), with a tail extending toward larger TKEL.

In Fig. 6.9 the experimental mass spectra are compared with the prediction of the code GRAZING [45]. Here, the experimental counts have been normalized to the calculated cross section for the one-proton stripping channel. The model [44] treats on the same footing quasi-elastic and deep inelastic processes. It takes into account the lower inelastic excitation of the colliding nuclei and considers in a simple way nucleon evaporation from the primary fragments. The program describes the transfer reaction as a sequence of independent single nucleon transfer modes. In the comparison with experimental mass distributions, one sees that there is in general a good agreement between data and theory for neutron pick-up transfer channels and for the isotopes belonging to the (-1p) channel. For the (-2p) channels discrepancies start to show up and this is more evident as the number of transferred protons increases. However GRAZING maintains a certain quantitative agreement on the very neutron-rich side of the isotope yields [27]. This is in fact the region closest to the neutron pick-up channels, whose behavior as a function of the number of transferred protons is much more regular than the corresponding one where neutron stripping channels are involved [27, 10].

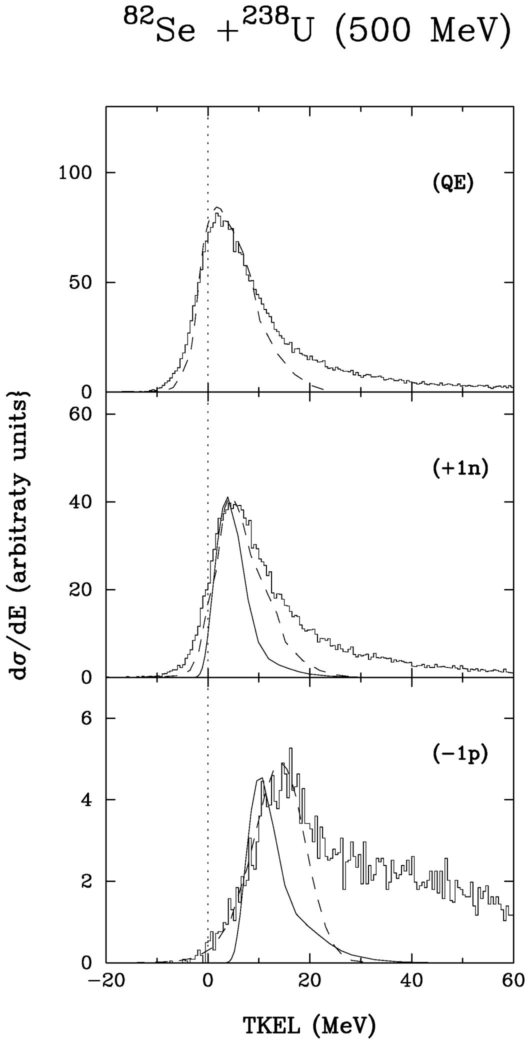

Figure 6.8: *Experimental TKEL distributions (histograms) for the quasi-elastic and the +1n, -1p channels. The dashed and the full lines are the GRAZING model predictions, with and without taking into account the 2% energy loss into the target.*

6.5 Conclusions

This preliminary analysis of the data set from reaction ^{82}Se+^{238}U shows the good quality of the tracking methods described in this thesis. It has been shown that individual nuclei populated via multinucleon transfer in this reaction, have been unambiguously identified in mass, ion charge and

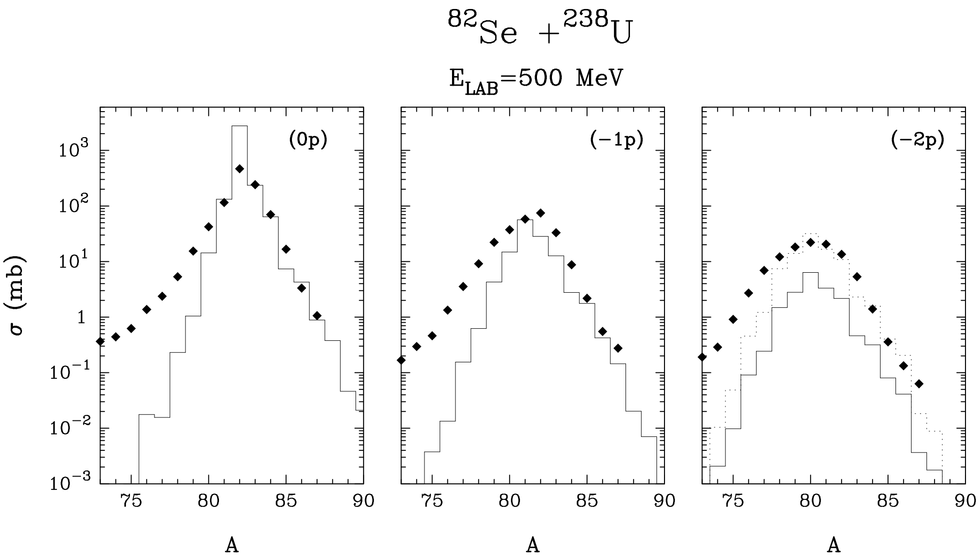

Figure 6.9: *Experimental vs. theoretical (GRAZING) total cross sections for the mass chains corresponding to* Z = 34 *(0p),* Z = 33 *(-1p-) and* Z = 32 *(-2p). Full and dashed lines are the theoretical calculations with and without the pairing interaction [44].*

nuclear charge. Energy (Q-value) spectra were derived from the data (with a resolution essentially depending only on the target thickness, and on the Mylar windows of the detectors). In particular, a good mass resolution of $\Delta A/A \cong 1/250$ has been reached, very near to the design value. Moreover, it was demonstrated that neutron-rich nuclei can be produced by multinucleon transfer reactions. One of the aims of this experiment was actually to populate the ^{78}Ni region. Looking at Fig. 6.10, it emerges that the difficulty in populating these extremely neutron-rich nuclei via multinucleon transfer reactions is not only due to the low primary cross section, but also to the fact

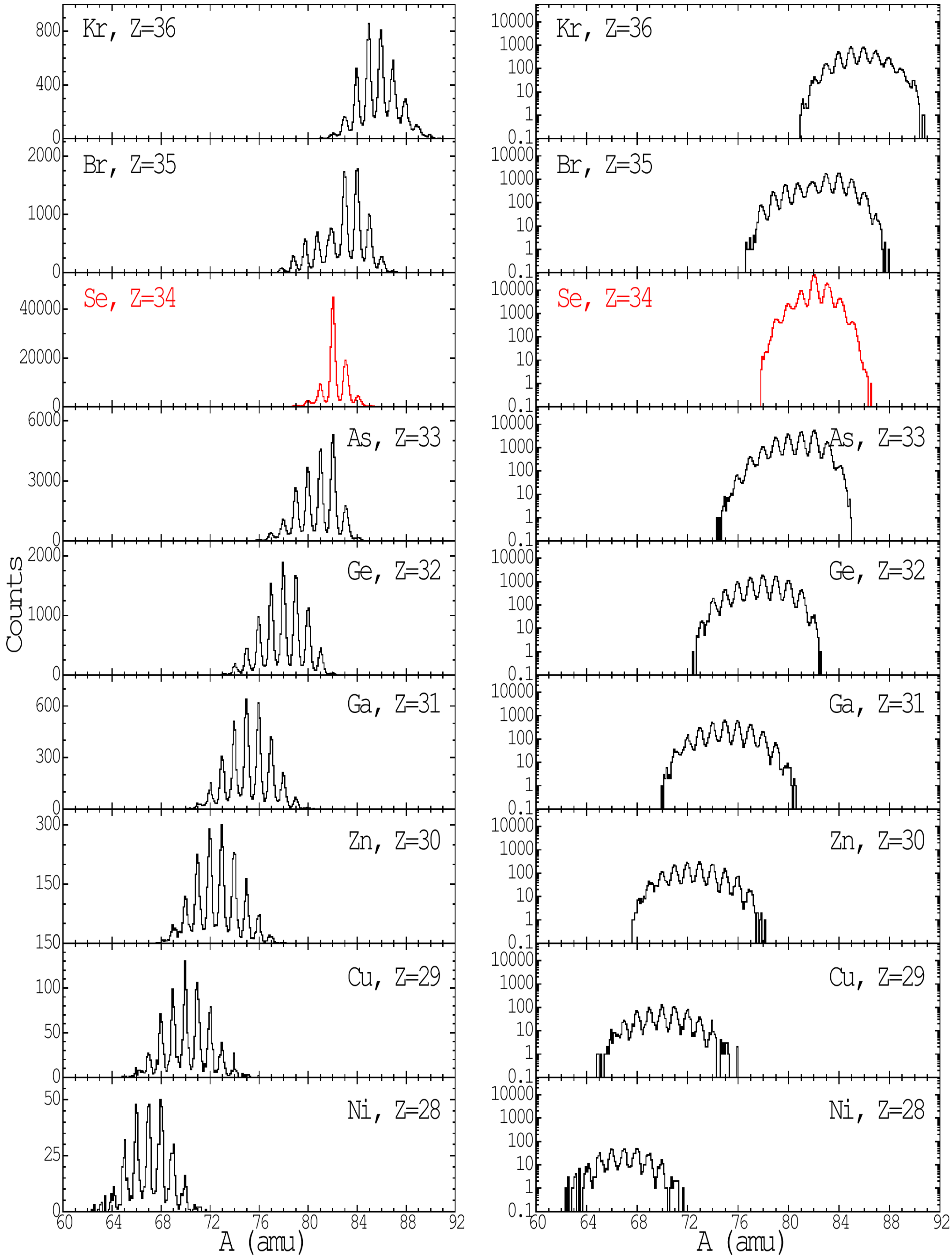

Figure 6.10: *Mass spectra for different Z in the reaction 505 MeV* ^{82}*Se on* ^{238}*U.*

that as more protons are stripped from the projectile, Q-values get more negative and neutron evaporation effects modify the final yields in a significant way. Effects of such nucleon evaporations from the primary fragments had already been shown to play an important role in such multinucleon transfer reactions (see [10] and references therein).

The information on the population of neutron-rich nuclei from the reaction ^{82}Se+^{238}U, will be extremely useful for further nuclear structures studies in this mass region, along the physical frame discussed at the beginning of this chapter.

Summary

The aim of this work was developing a suitable and reliable computer analysis procedure for the data taken in the experiments with the heavy-ion beams at the spectrometer PRISMA, recently installed at Laboratori Nazionali di Legnaro of INFN.

The most interesting features of PRISMA are a very large solid angle (80 msr) and momentum acceptance ($\pm 10\%$), good mass resolution (1/250) via (TOF) measurement, energy resolution up to 1/1000, and capability of rotation around the target in a wide angular range from -20^o to 130^o. PRISMA is based on a simple quadrupole-dipole magnet configuration, but the ion tracks are reconstructed event by event, via software, using the position, time and energy signals from the entrance detector, and from the array of focal plane detectors, on the basis of the detailed mapping of the magnetic fields.

The strength of this method lies is the mapping of the magnetic fields, which has been made through a “Finite Elements” approach tuned on the measured maps of the magnetic fields. This method leads to a realistic simulation of the fields even in their (non-negligible) fringing regions. All this software package has been framed into a user-friendly graphical interface.

Because of the difficulties of the problem in itself, as well as of the complexity of a set-up like PRISMA, the analysis has to deal with the ion tracking problem and with the physical case under study, but several other experimental issues (such as, for instance, electronics, heavy-ion detectors, data acquisition processes) have to be taken into account.

The procedure has been successfully applied to the data set from the reaction 505 MeV ^{82}Se+^{238}U, close to the grazing angle, recently studied at LNL. A very good result has been obtained in terms of mass resolution, as it is described in chapter 6 of this thesis. The results of this analysis allows the study of multinucleon transfer channels in this reaction, and preliminary results have been compared with the semi-classical model GRAZING.

Appendix A

A.1 Central trajectory coordinates reference

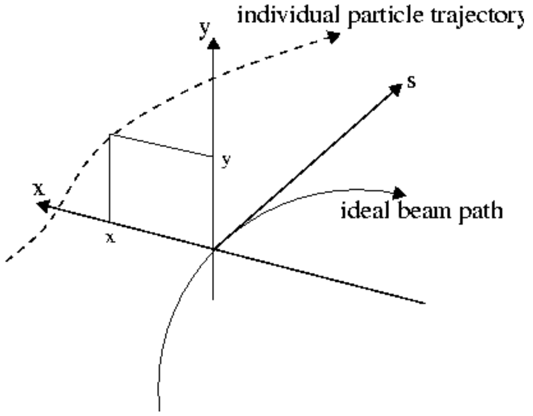

Figure A.1: *Coordinate system for particle motion in curved systems.*

It is common to use a fixed Cartesian coordinate reference system (x, y, z) to define the ideal ion path as determined by the Lorenz force. In most cases this ideal path is determined through the location of the deflection magnets along a system of magnetic fields. Once the ideal path is known and fixed, we are interested only in the deviation of individual particle trajectories from this ideal path. The natural reference system for curved trajectories is an orthogonal coordinate system (x, y, s) that follows an ideal particle traveling along the central path of the system (see Fig. A.1). It is convenient to use a the vector s for the coordinate along the ideal path in contrast to z in the fixed coordinate system. The transverse coordinates will measure only the deviations from the ideal path, that are assumed to be small in linear beam dynamics.

In this reference system, the motion of each individual particle is defined in the six-dimensional phase space formed by the three space coordinates (x, y, s) and the three momentum coordinates (p_x, p_y, p_s).

A.2 Example of the Over-Relaxation Method

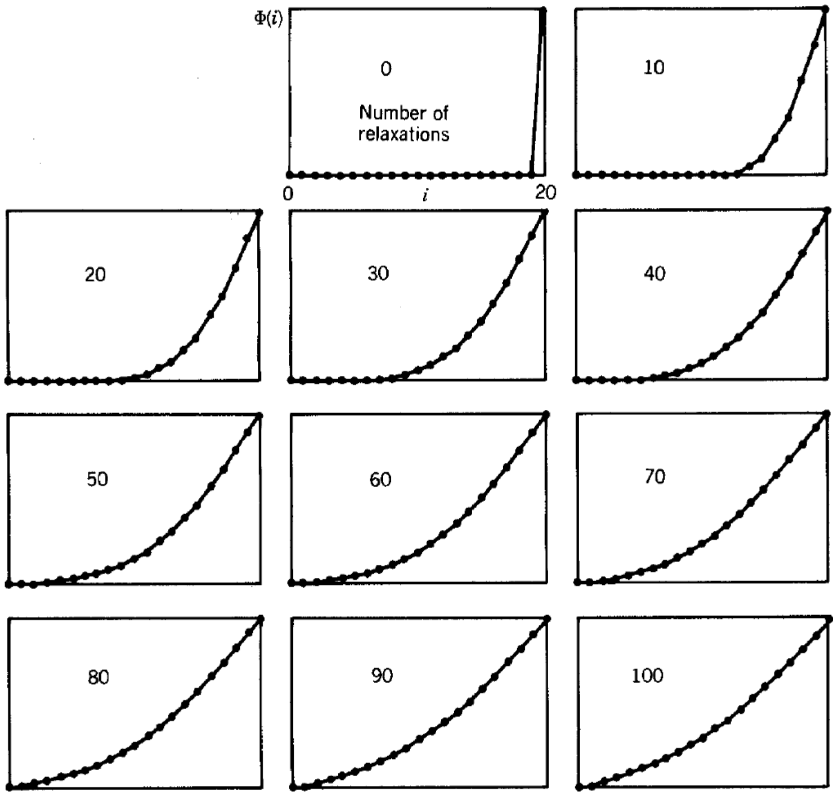

Figure A.2: *Relaxation method for solving the Laplace equation. Successive one-dimensional solutions for electrostatic potential between charged plates as a function of the number of mesh relaxations. Initial conditions:* $\Phi(0)..\Phi(19) = 0; \Phi(20) = 1$.

A.3 Table of Experimental Data

$Z = 28$

A	Counts
62	1
63	17
64	40
65	127
66	204
67	234
68	242
69	154
70	62
71	13
72	1

$Z = 29$

A	Counts
65	3
66	47
67	133
68	307
69	419
70	496
71	488
72	343
73	170
74	70
75	16
76	2

$Z = 30$

A	Counts
68	37
69	253
70	623
71	1067
72	1349
73	1339
74	1121
75	643
76	332
77	99
78	6

$Z = 31$

A	Counts
70	13
71	186
72	684
73	1448
74	2246
75	2870
76	2707
77	2038
78	1042
79	307
80	49
81	1

$Z = 32$

A	Counts
73	86
74	866
75	2107
76	4417
77	6821
78	8586
79	7777
80	5486
81	2165
82	189
83	1

$Z = 33$

A	Counts
74	1
75	42
76	365
77	2185
78	5980
79	13449
80	17443
81	21886
82	24370
83	9434
84	1508
85	57

$Z = 34$

A	Counts
78	115
79	3494
80	15998
81	49402
82	191580
83	100099
84	29638
85	4185
86	167
87	1

$Z = 35$

A	Counts
77	17
78	401
79	1432
80	2813
81	3692
82	5269
83	8744
84	8855
85	5259
86	1601
87	184
88	3

$Z = 36$

A	Counts
81	14
82	230
83	972
84	2454
85	4171
86	4351
87	3328
88	1843
89	696
90	171
91	2

Table A.1: *Mass distributions for different Z values from the ^{82}Se+^{238}U reaction. The counts observed for each (Z, A) pair are reported (see text).*

A.4 Example of Acquisition Program

A typical NEO++ program starts with the declaration of the data format of the incoming events and is followed by the acquisition loop, within which many useful operations on events may be stated by means of predefined data structures that ease the task of programmers.

The event description

Before introducing the input data format syntax, it is worth noticing that the specification of the incoming data format is equivalent to the specification of the present configuration of the spectrometer, or at least of that part of the configuration in which the user is interested in: hence, prior to any operation on events, it should be possible to express the type and number of parameters measured by each detector. That is why the first section of a NEO++ program should deal with the declaration of such parameters; for instance, the expression:

```
format(Ge_type)
        item energy;
        item time;
end_format
```

states that Germanium type detectors consists in two measured parameters (items). The item keyword declares the following identifier to be semantically equivalent to an `unsigned short`, for which all operations allowed on integer type variables hold (including explicit assignment). The syntax of the format statement follows:

```
format(detector_type_identifier)
        item_list
end_format
```

where `item_list` is a list of the items “measured” from that type of detector and is set up by a sequence of statements of the form:

```
item item_name;
```

The format declaration really defines a new data structure, but has not a physical variable associated with it, i.e. it cannot be addressed prior to a declaration of a variable of that type:

```
Ge_type a_germanium;
```

As usual for C language data structures, the items of the `a_germanium` variable may be addressed using the dot notation, so that the following code would compile correctly:

```
unsigned short us1, us2;

us1 = a_germanium.energy;
us2 = 3 * a_germanium.time + 2;
```

The `Detector` statement

The specification of the present configuration of the spectrometer is accomplished through the use of a number of Detector declarations like the following:

```
Detector <Ge_type, 40> ge;
```

which states that the spectrometer is set up with forty `Ge_type` detectors, each one measuring the two parameters declared in the previous format statement (energy and time). Addressing each one of the forty detectors is now straightforward; the syntax:

```
ge[7].energy
```

addresses the energy item of the eighth detector (the C language rule of numbering arrays starting from the zeroth element holds) in the collection of forty. It is worth underlining the fact that, with such a syntax, we have implicitly put an order relation on our collection of forty `Ge_type` detectors;

that is, each detector is now distinguishable of the others by means of its position in the array, a position that we will subsequently refer to as the key of the detector.

Bibliography

[1] A. P. A. Bracco. SPES Technical design report. *LNL Annual Report*, page 181/2002, 2002. `http://www.lnl.infn.it/~spes`.

[2] C. A. A. Thom. *Field Computations in Engineering & Physics.* D.Van Nostrand Company, Ltd., London, 1961.

[3] B. Back et al. Transport efficiency of the Argonne fragment mass analyzer. *Nuclear Instruments and Method in Physics Research*, A379:206–211, 1996.

[4] S. Beghini. *LNL Annual Report*, 160/2000:161, 1999.

[5] M. Bellato et al. *LNL Annual Report*, 178/2001:185, 2000.

[6] A. Bohr and B. Mottelson. *Nuclear Structure*, volume 1. W.A. Benjamin, Inc., New York, 1969.

[7] D. S. Burnett. *Finite Elements Analysis: From Concepts to Applications.* Addison-Wesley, New York, 1988.

[8] P. Butler. The SUSAN Working Party chaired by P.A. Butler: "Proposal for SUSAN". 1990.

[9] L. Corradi. *LNL Annual Report*, 139/1999:182, 1998.

[10] L. Corradi et al. *Physical Review*, C66:024606, 2002.

[11] L. Corradi et al. Neutron rich nuclei produced via multi-nucleon transfer in ^{82}Se+^{238}U. March 2003.

[12] H. Enge. Magnetic spectrographs for nuclear reaction studies. *Nuclear Instruments and Methods*, 162:161–180, 1979.

[13] H. Fullbright et al. *Nuclear Structure Laboratory Annual Report*, 1973.

[14] A. Gadea et al. Coupling a CLOVER detector array with the PRISMA magnetic spectrometer. *The European Physical Journal*, A20:193, 2004.

[15] M. Galassi et al. *GNU Scientific Library Reference Manual.* Paperback, 2003.

[16] `http://gasp.lnl.infn.it/index.htm`.

[17] F. Golding. *Treatise on Heavy-Ion Science*, volume 7. D.A. Bromley, New York, 1985.

[18] C. Gross. Performance of the Recoil Mass Spectrometer and its detector systems at the Holifield Radioactive Ion Beam Facility. *Nuclear Instruments and Method in Physics Research*, A450:12–29, 2000.

[19] I. Hamamoto et al. *Nuclear Physics*, A683:255, 2001.

[20] D. Hendrie et al. *Bulletin of American Physical Society*, 15:650, 1970.

[21] S. Humphries. *Principles of Charged Particle Acceleration.* John Wiley and Sons, Ltd., 1999.

[22] D. Hutcheon et al. The DRAGON facility for nuclear astrophysics at TRIUMF-ISAC: design, construction and operation. *Nuclear Instruments and Method in Physics Research*, A498:190–210, 2003.

[23] H. Ikezoe et al. JAERI recoil mass separator. *Nuclear Instruments and Method in Physics Research*, A376:420–427, 1996.

[24] C. Jiang et al. *Physics Review*, C57:2393–2400, 1998.

[25] G. Lalazissis et al. *Physics Letters*, B418:7, 1998.

[26] D. Larson et al. *General Ion Optics Systems*, 1987.

[27] L.Corradi et al. *Physical Review*, C59:261, 1999.

[28] `http://www.lnl.infn.it/accelerators/accelerators.html`.

[29] `http://nnsa.dl.ac.uk/MIDAS/`.

[30] G. Montagnoli. *LNL Annual Report*, page 152, 2000. NIM-A in preparation.

[31] G. Montagnoli. The time-of-flight spectrometer for heavy ions PISOLO. *Nuclear Instruments and Methods in Physics Research*, A454:306–314, 2000.

[32] R. Nayac. *Physical Review*, C60:064305, 1999.

[33] `http://eballwww.in2p3.fr/EB/`.

[34] O. Odland. *Nuclear Instruments and Methods in Physics Research*, A378:149, 1996.

[35] H. E. S. Kowalski. RAYTRACE. July 1987.

[36] H. Savajois. VAMOS: A variable mode high acceptance spectrometer for identifying reaction products induced by SPIRAL beams. *Nuclear Instruments and Method in Physics Research*, B204:146, 2003.

[37] D. Schull. *The GSI Magnetic Spectrometer*. GSI, Darmstadt, 1983.

[38] C. Signorini et al. Performance of the LNL recoil mass spectrometer. *Nuclear Instruments and Method in Physics Research*, A339:531–542, 1994.

[39] A. Sinha et al. Heavy ion reaction analyzer (HIRA): a recoil mass separator facility at NSC. *Nuclear Instruments and Method in Physics Research*, A339:543–549, 1994.

[40] SPES Study Group. Project Study of an advanced facility for Exotic Beams at LNL. *LNL Annual Report*, page 149/99, 1999.

[41] A. Stefanini et al. The heavy-ion magnetic spectrometer PRISMA. *Nuclear Physics*, A701:217–221, 2002.

[42] S. Szilner et al. Search for pairing-vibration states of even Ca isotopes in ^{40}Ca +^{208}Pb transfer reactions. *The European Physical Journal*, A21:87, 2004.

[43] I. Talmi. Effective interactions and coupling schemes in nuclei. *Nuclear Physics*, A570:319–327, 1994.

[44] A. Winther. Dissipation, Polarization and Fluctuation in Grazing Heavy-Ion Collisions and the Boundary to the Chaotic Regime. *Nuclear Physics*, A594:203, 1995.

[45] A. Winther. GRAZING computer code. 1998.

[46] A. Wittkower and H. Betz. *Atomic Data*, 1973.

[47] H. Wollnik. *Optics of Charged Particles.* Academic Press, Orlando, FL, 1988.

[48] J. Ziegler. *The Stopping and Range of Ions in Solids*, volume 1. Pergamon Press, New York, 1985.